AGU PUBLICATIONS

JGR

Journal of Geophysical Research: Solid Earth

RESEARCH ARTICLE
10.1002/2016JB013692

Key Points:
- Attenuation tomography of the inner core performed from a global data set of waveform correlated measurements
- Complex regional variations of attenuation
- The observed pattern of attenuation is not in agreement with commonly accepted spherical degree 1

Supporting Information:
- Supporting Information S1
- Data Set S1
- Data Set S2

Correspondence to:
T. Pejić,
tanja.pejic@anu.edu.au

Citation:
Pejić, T., H. Tkalčić, M. Sambridge, V. F. Cormier, and R. Benavente (2017), Attenuation tomography of the upper inner core, *J. Geophys. Res. Solid Earth*, *122*, 3008–3032, doi:10.1002/2016JB013692.

Received 28 OCT 2016
Accepted 22 MAR 2017
Accepted article online 4 APR 2017
Published online 27 APR 2017

Attenuation tomography of the upper inner core

Tanja Pejić[1], Hrvoje Tkalčić[1], Malcolm Sambridge[1], Vernon F. Cormier[2], and Roberto Benavente[1,3]

[1]Research School of Earth Sciences, Australian National University, Canberra, ACT, Australia, [2]Department of Physics, University of Connecticut, Storrs, Connecticut, USA, [3]National Research Center for Integrated Natural Disaster Management, Santiago, Chile

Abstract The solidification of the Earth's inner core shapes its texture and rheology, affecting the attenuation and scattering of seismic body waves transmitted through it. Applying attenuation tomography in a Bayesian framework to 398 high-quality PKIKP waveforms, we invert for the apparent Q_p for the uppermost 400 km below the inner core boundary at latitudes 45°S to 45°N. We use damping and smoothing for regularization of the inversion, and it seems that the smoothing regularization combined with the discrepancy principle works better for this particular problem of attenuation tomography. The results are consistent with a regional variation in inner core attenuation more complex than hemispherical, suggesting coupling between inner core solidification and the thermal structure of the lowermost mantle.

1. Introduction

It is generally agreed that the inner core exhibits hemispherical heterogeneity in velocity and attenuation in its uppermost part, first reported by *Tanaka and Hamaguchi* [1997] and later confirmed by many studies [e.g., *Creager*, 1999; *Niu and Wen*, 2001; *Cao and Romanowicz*, 2004a, 2004b; *Yu and Wen*, 2006; *Tanaka*, 2012]. However, differences exist between the details of attenuation and velocity profiles in all of these studies [see, e.g., *Niazi and Johnson*, 1992; *Bhattacharyya et al.*, 1993; *Souriau and Roudil*, 1995; *Souriau and Romanowicz*, 1996; *Li and Cormier*, 2002]. The hemispheres were first defined by *Tanaka and Hamaguchi* [1997]: Eastern Hemisphere extends from 44°E to 177°E, and the Western Hemisphere extends from 183°W to 43°E. Studies focused on lateral variation of attenuation and velocity in the inner core often report slightly different locations for these boundaries, as *Irving and Deuss* [2011] show in their Table 1.

Our Table 1 summarizes some relevant studies on the attenuation of the inner core. Some earlier results suggested that Q_p in the inner core changes from about 200 to 1000 going from the top of the inner core to the center [*Doornbos*, 1974, 1983; *Cormier*, 1981; *Shearer and Masters*, 1990]; however, this depth dependency is not well resolved [*Bhattacharyya et al.*, 1993]. *Wen and Niu* [2002] studied the attenuation structure along equatorial paths (the paths that make an angle with Earth's rotation axis of more than 40°) in the top 80 km of the inner core. They found an average Q_p value of 250 in the Eastern Hemisphere and an average Q_p value of 600 in the Western Hemisphere. They showed that high attenuation also correlates with high velocities and vice versa. *Cao and Romanowicz* [2004b] performed direct measurements of PKIKP to PKiKP amplitude ratio in epicentral distance range of 134° to 144°. They confirmed hemispherical differences in velocity and attenuation up to 85 km below the inner core boundary (ICB) with higher attenuation in the Eastern Hemisphere (average Q_p of 160) than in the Western Hemisphere (average Q_p of 335). They argue for a transition zone in the Eastern Hemisphere, where Q_p changes from decreasing with depth to increasing with depth between ~32 and ~85 km below the ICB. In the Western Hemisphere this pattern is not observed, and in the same depth range Q_p decreases slightly. According to *Singh et al.* [2002] Q_p decreases with increasing melt fraction. This leads to the conclusion that (liquid) melt inclusions may be well isolated in the Eastern Hemisphere while better connected in the Western Hemisphere resulting also in higher porosity. They suggest that this kind of pattern is probably caused by hemispherical temperature differences across the ICB concluding that on the cold western side a faster freezing rate leads to higher porosity.

Yu and Wen [2006] oppose this transition zone claiming that synthetic PKIKP amplitudes based on such complex models cannot be distinguished from a model with a constant Q_p value of 600 for Western Hemisphere, and a constant Q_p value of 300 for Eastern Hemisphere. They joint fit the observed PKIKP/PKiKP and

Table 1. Some of the Relevant Studies on Inner Core Attenuation[a]

Study	Distance Range	Results
Niazi and Johnson [1992]	140°–170°	$Q_p = 175 \pm 10$
Bhattacharyya et al. [1993]	146.4°–153.9°	$Q_p = 286$ time domain; $Q_p = 357$ frequency domain
Souriau and Roudil [1995]	149°–160°	$Q_p = 200 - 440$
Li and Cormier [2002]	150°–180°	$Q_p = 307 \pm 90$
Wen and Niu [2002]	120°–141°	$Q_p = 600$ west; $Q_p = 250$ east
Cao and Romanowicz [2004b]	134°–144°	$Q_p = 335$ west; $Q_p = 160$ east
Yu and Wen [2006]	132°–141° and 146°–151°	$Q_p = 600$ west; $Q_p = 300$ east
Iritani et al. [2010]	≈135°–162°	$Q_p = 180 - 370$ west only
Tanaka [2012]	150°–160°	$Q_p = 300$–400 west; $Q_p = 180$–1000 east
Attanayake et al. [2014]	129°–141°	$Q_p = 150 - 1000$
Iritani et al. [2014a]	135°–160°	$Q_p \approx 150 - 1000$

[a] Q_p values given are the average for the entire upper inner core, unless otherwise stated. All of the single values and ranges are given for a particular depth extent limited by the designated epicentral distance range. The reader is referred to the text and original sources for more details.

PKIKP/PKPbc amplitude ratios in epicentral distance range of 131°–141° and 146°–151°, respectively. The amplitude ratios are consistently smaller for data sampling the Eastern Hemisphere than those corresponding to data sampling the Western Hemisphere. The data require a change of Q_p with depth in the Eastern Hemisphere, whereas there is no evidence of depth dependence of Q_p in the Western Hemisphere. Instead of a transition zone, *Yu and Wen* [2006] propose simple attenuation models for both hemispheres arguing for an average Q_p value of 300 in the top 300 km and an average Q_p value of 600 in the deeper portions of the Eastern Hemisphere. For Western Hemisphere they give an average Q_p value of 600 in the top 375 km. Since high attenuation correlates with the high velocities they observed, and vice versa, they explain this behavior by different alignments of hexagonal close packed (hcp) iron crystals, with the hypothesis that axis of high (low) velocity corresponds to that of high (low) attenuation. While this mechanism may readily explain the attenuation structure in the Western Hemisphere, it would require an alignment that would cancel the pressure effect such that the seismic velocity does not increase in the top 235 km in the Eastern Hemisphere. They state that it is possible that factors such as partial melt may play a big role in generating this anomalous top layer in the Eastern Hemisphere.

Their results agree well with those of *Tanaka* [2012] who argues for 250 km thick layer of high attenuation in the Eastern Hemisphere and a layer of constant Q_p in the Western Hemisphere even though his Q_p values for these layers are lower. The most important difference between his study and the one of *Cao and Romanowicz* [2004b] is the thickness of hemispherical layers for velocity and attenuation structure, particularly for the Eastern Hemisphere where he advocates layers that are 3 to 4 times thicker. He also proposed that the Q_p structure is more complicated, with layers of constant Q_p in the Western Hemisphere and of lower Q_p in the thicker Eastern Hemisphere.

Iritani et al. [2010] have employed a waveform inversion method for attenuation parameters based on simulated annealing. They obtained attenuation models for the northeastern Pacific region, using equatorial paths from events concentrated in South America. Their results are generally consistent with the results of *Wen and Niu* [2002] and reveal a gradual increase of attenuation with depth. They point to a moderate attenuation ($Q_p = 370$) at the top of the inner core and an increase down to a depth of 200–250 km below the ICB where attenuation reaches its peak ($Q_p = 180$) and a decrease to a depth of 450–500 km below the ICB where the attenuation becomes insignificant. They propose different crystallization rates to explain hemispherical variation in the inner core and possible convection motion to explain gradual change of attenuation with depth.

Attanayake et al. [2014] have shown that what was previously thought of as the Western Hemisphere has more complicated structure. Using PKIKP and PKiKP data and distributing them in eight bins, they have shown that

the uppermost 80 km of the inner core has a degree 2 heterogeneity. Their results also showed that the zone of high attenuation extends into the central Pacific region and has reverse (mantle-like) correlation with velocity. These findings are later confirmed by *Iritani et al.* [2014a, 2014b], who again use waveform inversion based on simulated annealing but with global data this time. They used differential travel times and amplitude ratios between PKIKP and PKPbc or PKPcd (PKiKP) phases covering a distance range from 135° to about 160°. Their results are generally consistent with those of *Attanayake et al.* [2014], the only difference being that their data cover a wider range of distance and so their models extend deeper in the inner core. They observe that all hemispherical differences disappear 300 km below the ICB.

1.1. Suggested Mechanisms of Inner Core Dynamics

There are many interpretations to hemispherical heterogeneity within the inner core, consistent with melting or freezing in both hemispheres. In either case there are different ways of interpreting results reported by various observations, specifically the positive correlation between seismic velocities and attenuation. Current debates mostly concentrate on whether attenuation is mostly intrinsic or due to scattering and the mechanisms needed to explain this. *Aubert et al.* [2008] and *Gubbins et al.* [2011] propose that the inner core growth is coupled to the core-mantle boundary thermally. Solidification texturing is proposed as the most likely mechanism for explaining seismic heterogeneities below the inner core boundary. Slower freezing rate would result in widely spaced dendrites, sensitive to the flow direction, and produce a more textured solid through preferential fast axis orientation of iron crystals (for more details and a recent review, see *Tkalčić* [2015]). Faster freezing rate would inhibit this effect resulting in a solid with more random dendrite orientation. Seismic waves propagating through the inner core would thus be faster on average and more attenuated in the less textured, fast-growing regions (the Eastern Hemisphere) and would have more anisotropic wave speed and attenuation in the more textured, slow-growing region (the Western Hemisphere). *Monnereau et al.* [2010] and *Alboussière et al.* [2010] proposed that degree 1 heterogeneity is the consequence of differential scattering across the two hemispheres due to convectional translation of material from western to Eastern Hemisphere. These models, however, cannot predict the lateral heterogeneity observed in *Attanayake et al.* [2014] and *Iritani et al.* [2014a]. This is pointing to solidification processes more complex than previously thought.

1.2. This Study

In this study we perform attenuation tomography of the upper inner core, for about 400 km below the ICB. As far as we are aware this is the first study where attenuation tomography has been performed for the inner core, and with it we aim to advance the ongoing debate about attenuation and possible geodynamic scenarios in place. In section 2 we present our data set and introduce the measurement technique. This is followed by a description of the tomography problem and probabilistic approach used to solve it in section 3. The synthetic tests and results are shown in sections 4 and 5, respectively. We conclude with the discussion of the results in section 6.

2. Data and Measurements

Quality factor Q_p is a dimensionless physical quantity used to measure attenuation. This factor is defined as the average energy loss per oscillation cycle or alternatively as the amount of work done per oscillation cycle, and as such it is inversely proportional to attenuation. We can define the inverse of Q_p as

$$Q_p^{-1}(\omega) = \Delta \int_{-\infty}^{\infty} D(\tau) \frac{\omega\tau}{1+\omega^2\tau^2} \mathrm{d}\tau, \tag{1}$$

where ω is the oscillation frequency of the propagating wave, τ is a characteristic relaxation time, $D(\tau)$ is the retardation spectrum, and Δ is the modulus defect. The modulus defect is a measure of total reduction in shear modulus that is obtained in going from low temperature to high temperature. The Q_p factor is commonly measured from the spectral amplitude ratio of two neighboring (i.e., closely related) phases. Presenting the logarithm of these ratios against frequency plots a line, and the slope of this line is used to estimate Q_p (see *Niazi and Johnson* [1992] for an example). With this formulation the only frequency-dependent part of the spectral ratio comes from inelastic attenuation. The entire attenuation is estimated purely from the amplitudes of the associated phases, while the broadening of the wave pulse and distortion of its shape due to attenuation are not taken into account. A more comprehensive approach would be to estimate attenuation from the shape and amplitude of the waveform rather than just the amplitude.

This is why in this study we use *SAWIB* (Simulated Annealing Waveform Inversion of Body Waves) algorithm [*Garcia et al.*, 2013], based on simulated annealing approach [*Chevrot*, 2002], to measure the t^* parameter. This quantity is defined as

$$t^* = \int \frac{\mathrm{d}t}{Q_p} \approx \sum_{i=1}^{N} \frac{\Delta t_i}{Q_p}, \tag{2}$$

integrated over a raypath. Δt_i is the total traveltime of path segment i through a region of constant Q_p. The t^* parameter is inversely proportional to Q_p and directly proportional to attenuation. SAWIB uses a nonlinear waveform inversion method to perturb a number of parameters (see *Garcia et al.* [2013] for details), one of which is the t^* parameter. These parameters are used within the algorithm to model the waveforms that best fit the observed ones according to a simulated annealing algorithm. In this context, we model three main core phases: PKIKP, PKPbc, and PKPab. Only PKIKP and PKPbc are used to estimate attenuation within the inner core. We choose PKPbc to be our reference phase as it has similar raypath to the inner core sensitive phase PKIKP. The two phases leave the source at almost identical angles and have similar paths through the mantle. The attenuation in the outer core is negligible compared to the inner core. We can use PKPbc and PKIKP phases to estimate the attenuation effect of the inner core. Due to the raypath similarity of these two phases within the mantle and the outer core, we can assume that any differential effect visible on the PKIKP phase is strictly caused by the structure of the inner core. Furthermore, while corrections for the lower mantle are commonly applied in travel time studies of the lowermost mantle and the inner core, there is presently no consensus on the Q_p structure of the lowermost mantle. Hence, we do not apply any corrections to our t^* estimates as we believe this would only contribute to the uncertainties of our models.

The model waveforms can be represented as a sum of individual phases [*Garcia et al.*, 2004]:

$$S_i(t) = W_{ij}^{bc}(t) * \mathrm{Att}(t_{ij}^*, t) + W_{ij}^{bc}(t) + H \cdot W_{ij}^{bc}, \tag{3}$$

where W_{ij}^{bc} is PKPbc waveform j recorded at station i, with all the relative amplitude corrections and geometrical spreading amplitude corrections included. $\mathrm{Att}(t_{ij}^*, t)$ is the attenuation operator acting on the reference phase, and H is a Hilbert transform acting on the reference phase. The attenuation operator is a function of t^*, and in frequency domain it is given by

$$\mathrm{Att}(t^*, f) = \exp\left(-\pi f t^*\right) \exp\left[-2if \ln\left(\frac{f}{f_0}\right) t^*\right], \tag{4}$$

with the reference frequency f_0 (set to 0.5 Hz). In this formulation the quality factor Q_p and t^* are nearly constant in a band of frequencies [*Futterman*, 1962; *Carpenter*, 1966; *Anderson and Hart*, 1977]. The three terms in equation (3) therefore describe the reference PKPbc phase, the PKIKP phase as an attenuated version of the reference phase, and PKPab phase as a Hilbert transform of the reference phase, respectively.

The SAWIB algorithm was used on 50 globally distributed events (Table 2), and the t^* parameter has been estimated for 398 records in total. We focused on the records that show clear PKP arrivals in displacement seismograms when unfiltered. We avoided filtering because we are fitting the shape of the incoming waves rather than just the amplitude and filters may affect this shape. We used events of magnitude between 5.5 and 7 and deeper than 100 km. There are a few exceptions in the data set (larger and/or shallower events) that were chosen purely because of the clear PKP arrivals with relatively simple source-time functions (which affects the SAWIB algorithm) or unobstructed by depth phases. We decided to use strictly PKIKP and PKPbc phases, and our data set spans the epicentral distances between 147° and 155°. The raw seismograms of PKP waves were thus used as an input for the SAWIB algorithm. All the traces were downloaded from the Incorporated Research Institutions for Seismology Data Management Center (IRIS DMC) database.

The examples of the observed waveforms and their optimal fit according to the SAWIB algorithm are shown in Figure 1, and the estimated t^* parameters and the resulting coverage of the inner core are shown in Figure 2. Most of our t^* estimates are in the range between 0.01 and 1.2 s. There are, however, a number of larger estimates and a few observations having values on the order of 2 and 3 s. When these data are plotted on a scale encompassing the full range of estimated values, it is impossible to see the global variety of t^* parameters because of the majority of them plotting on the lower end of the color scheme, while a few larger values stand out in a drastically different color. We choose then to set the boundaries of our color scale to represent the range of the majority of our estimates, while those estimates that are larger than the ones shown are plotted in gray. We point the reader to some of those gray filled circles in Figure 2 showing large t^* estimates in

Table 2. List of Earthquakes Used in This Study[a]

Date	Time	Location (Latitude, Longitude)	Depth (km)	Magnitude
20/3/1993	09:20:34	−56.1°, −27.8°	125.3	M_w 6.3
5/11/1996	09:41:31	−31.22°, −179.96°	340.7	M_w 6.8
12/4/1997	09:21:47	−28.10°, −178.32°	98.5	M_w 6.0
3/5/1997	16:45:55	−31.64°, −179.34°	47.8	M_w 6.9
8/10/1998	04:51:40	−16.05°, −71.35°	111.6	M_w 6.2
2/3/1999	17:45:54	−22.80°, −68.49°	110.2	M_w 5.9
14/6/2000	02:15:28	−25.63°, 178.06°	631.2	M_w 6.4
18/12/2000	01:19:21	−21.15°, −179.12°	617.7	M_w 6.5
12/9/2001	08:48:37	−21.02°, −179.10°	610.6	M_w 6.4
10/2/2002	01:47:07	−55.98°, −29.15°	198.0	M_w 5.9
16/6/2002	06:55:13	−17.92°, −178.65°	571.2	M_w 5.9
24/9/2002	03:57:20	−31.45°, −69.14°	104.6	M_w 6.3
12/11/2002	01:46:49	−56.58°, −27.72°	118.8	M_w 6.2
17/11/2002	04:53:55	47.8°, 146.0°	483.9	M_w 7.3
27/4/2003	22:57:44	−81.68°, −71.58°	553.3	M_w 6.0
21/7/2003	13:53:59	−5.50°, 148.81°	196.6	M_w 6.4
17/9/2003	21:34:47	−21.43°, −68.27°	126.1	M_w 5.8
25/1/2004	11:43:10	−16.85°, −174.17°	129.6	M_w 6.7
10/6/2004	15:19:56	55.7°, 160.0°	187.4	M_w 6.9
14/8/2005	02:39:39	−19.7°, −69.11°	114.6	M_w 5.8
9/9/2005	11:26:05	−31.6°, −69.1°	114.0	m_b 5.8
2/1/2006	22:13:40	−19.97°, −178.11°	584.1	M_w 7.1
26/2/2006	03:08:28	−23.67°, −179.95°	534.3	M_w 6.4
7/3/2006	06:28:55	−14.85°, 167.36°	138.9	M_w 6.2
30/4/2006	08:17:35	−15.11°, 167.40°	134.1	M_w 6.1
27/6/2006	02:59:16	−19.96°, −178.23°	574.9	M_b 6.0
22/9/2006	02:32:24	−26.85°, −63.11°	583.0	M_w 6.0
29/4/2007	12:41:58	52.0°, −180.0°	126.9	M_w 6.2
6/5/2007	21:11:53	−19.47°, −179.32°	678.6	M_w 6.5
21/7/2007	13:27:03	−8.09°, −71.21°	633.7	M_w 6.0
31/7/2007	02:42:49	−56.10°, −27.73°	113.3	M_w 5.7
26/9/2007	04:43:18	−3.96°, −79.22°	102.1	M_w 5.9
5/10/2007	07:17:54	−25.20°, 179.45°	521.3	M_w 6.5
19/11/2007	00:52:12	−21.21°, −178.67°	558.9	M_w 6.3
15/12/2007	08:03:16	−7.62°, 127.51°	181.0	M_w 6.0
12/2/2008	12:50:19	16.43°, −94.24°	85.7	M_w 6.5
12/10/2008	20:55:41	−20.20°, −65.0°	357.8	M_w 6.1
22/11/2009	07:48:21	−17.82°, −178.37°	526.8	M_w 6.3
4/3/2010	22:39:25	−22.27°, −68.46°	108.4	M_w 6.3
11/4/2010	22:08:11	37.0°, −3.5°	619.6	M_w 6.3
23/5/2010	22:46:51	−14.00°, −74.43°	102.6	M_w 6.1
24/5/2010	16:18:28	−8.12°,−71.64°	582.1	M_w 6.5
17/6/2010	13:06:51	−33.19°, 179.78°	211.1	M_w 6.0
30/6/2010	04:31:01	−23.29°, 179.18°	572.8	M_w 6.4
12/7/2010	00:11:20	−22.28°, −68.32°	109.4	M_w 6.2
16/8/2010	19:35:48	−20.84°, −178.76°	600.8	M_w 6.2
25/2/2011	13:07:26	17.8°, −95.2°	130.6	M_w 6.0

Table 2. (continued)

Date	Time	Location (Latitude, Longitude)	Depth (km)	Magnitude
29/7/2011	19:35:48	−23.7°, 179.8°	522.8	M_w 6.7
1/6/2012	05:07:01	−77.1°, −148.9°	12.0	M_w 5.5
26/10/2015	09:09:42	−36.4°, 70.7°	231.0	M_w 7.5

[a]Dates are formatted as day/month/year.

East Asia and in the Indian Ocean, and a few in central America and off the west coast of North America. It is interesting to see that larger estimates around the Americas occur along the polar paths. This is also observed in the Indian Ocean, where a few polar paths are showing larger attenuation estimates than the equatorial ones (with two exceptions of larger estimates along equatorial paths) in approximately the same region of the Indian Ocean. While these observations may point to anisotropy of attenuation, with polar paths seemingly more attenuated than the equatorial ones, we do not think that our data set provides a good enough resolution to address this problem. We focus on the lateral variation of Q_p in the uppermost inner core instead. A number of t^* estimates off the coasts of North and Central America are along these anomalous paths and larger than 1.0. This should be kept in mind when interpreting results, as removing those paths from the inversion would eventuate in lower attenuation than in the present maps in that region. Anisotropy of attenuation could be the focus of future work, using a data set that spans a greater range of epicentral distances and thus providing better resolution.

3. Tomographic Inversion

To perform attenuation tomography of the inner core, we rewrite equation (2) in matrix form:

$$\begin{bmatrix} t_1^* \\ t_2^* \\ \vdots \\ t_D^* \end{bmatrix} = \begin{bmatrix} \frac{\Delta l_{11}}{v_{11}} & \frac{\Delta l_{12}}{v_{12}} & \cdots & \frac{\Delta l_{1N}}{v_{1N}} \\ \frac{\Delta l_{21}}{v_{21}} & \frac{\Delta l_{22}}{v_{22}} & \cdots & \frac{\Delta l_{1N}}{v_{2N}} \\ \vdots & & \ddots & \vdots \\ \frac{\Delta l_{D1}}{v_{D1}} & \frac{\Delta l_{D2}}{v_{D2}} & \cdots & \frac{\Delta l_{DN}}{v_{DN}} \end{bmatrix} \cdot \begin{bmatrix} Q_{p_1}^{-1} \\ Q_{p_2}^{-1} \\ \vdots \\ Q_{p_N}^{-1} \end{bmatrix}. \tag{5}$$

The t^* vector on the left-hand side of equation (5) is our data vector **d**, and the ${Q_p}^{-1}$ vector on the right-hand side is our unknown model vector **m**. The matrix relating the two is the kernel matrix **G**. It is a matrix of total traveltimes through the inner core. The core is parameterized as N blocks (parameters) 45° wide. Δl_{DN} and v_{DN} are the length of the Dth raypath segment through the Nth block of the inner core, and the average velocity of the wave along that segment, respectively. We use ak135 velocity model [*Kennett et al.*, 1995] to compute v_{DN}, travel times through the inner core, and consequently Δl_{DN}.

Since Q_p factor is a nonnegative physical quantity, inverting directly for it or its inverse puts us in an unwelcome situation of getting an inversion solution which just might contain negative or zero values of Q_p for the inner core. Another, less obvious, problem with the attenuation tomography formulated in this way is that we expect much bigger deviations of the Q_p factor from some reference value than in the case of, for example, velocity tomography. We use Newton's continuous gradient method to find the solution vector. Iterative methods like Newton's method use small steps to move away from the starting guess and find a minimum of the cost function; hence, large deviations from that starting position will make it difficult, if not impossible, for the algorithm to converge. To circumvent these two problems, we invert for the logarithm of inverse Q_p. In doing so we guarantee positivity as the logarithm of a negative number does not exist. While this transformation makes it safer to invert for the Q_p factor, it also makes the inversion problem nonlinear, so we need to introduce a few approximations to linearize the problem before we can employ optimization to solve it.

With this transformation, the system of equations we are trying to solve becomes

$$\begin{bmatrix} t_1^* \\ t_2^* \\ \vdots \\ t_D^* \end{bmatrix} = \begin{bmatrix} \frac{\Delta l_{11}}{v_{11}} & \frac{\Delta l_{12}}{v_{12}} & \cdots & \frac{\Delta l_{1N}}{v_{1N}} \\ \frac{\Delta l_{21}}{v_{21}} & \frac{\Delta l_{22}}{v_{22}} & \cdots & \frac{\Delta l_{1N}}{v_{2N}} \\ \vdots & & \ddots & \vdots \\ \frac{\Delta l_{D1}}{v_{D1}} & \frac{\Delta l_{D2}}{v_{D2}} & \cdots & \frac{\Delta l_{DN}}{v_{DN}} \end{bmatrix} \cdot \begin{bmatrix} \exp(m_1) \\ \exp(m_2) \\ \vdots \\ \exp(m_N) \end{bmatrix}, \tag{6}$$

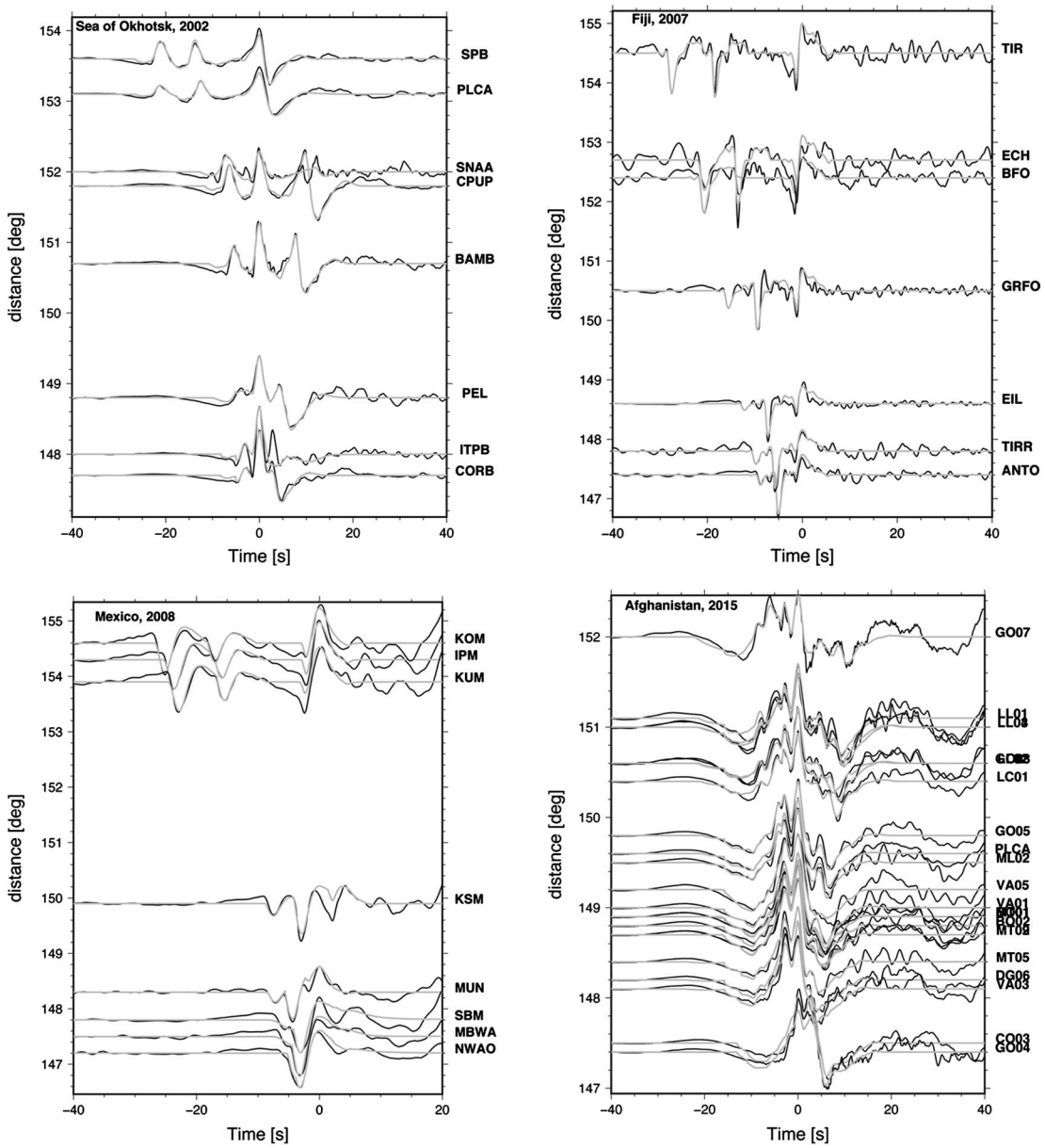

Figure 1. Examples of waveform fit using the SAWIB algorithm for four events. Observed traces are shown in black line, and the modeled traces are shown in gray line. The traces are centered on the theoretical PKPab arrival time.

where $m_i = \ln\left(Q_{p_i}^{-1}\right)$ denotes a natural logarithm of ith nonlinear parameter. We will assume now that our measurements are independent of each other and that the knowledge of any one observation of the t^* parameter does not affect our knowledge about any other t^* parameter. This is a reasonable assumption since our measurements are obtained through the SAWIB algorithm independently for each event. The events are distributed globally, and there is no reason to believe that one measurement is connected to another. We assume that the errors on the measurements are described by an uncorrelated Gaussian process.

3.1. Probabilistic Framework and Least Squares

The approach we are taking here to perform the inversion is adopted from *Benavente* [2016] and relies on Bayes' theorem:

$$P(\mathbf{m}|\mathbf{d}) \propto P(\mathbf{d}|\mathbf{m}) \times P(\mathbf{m}), \tag{7}$$

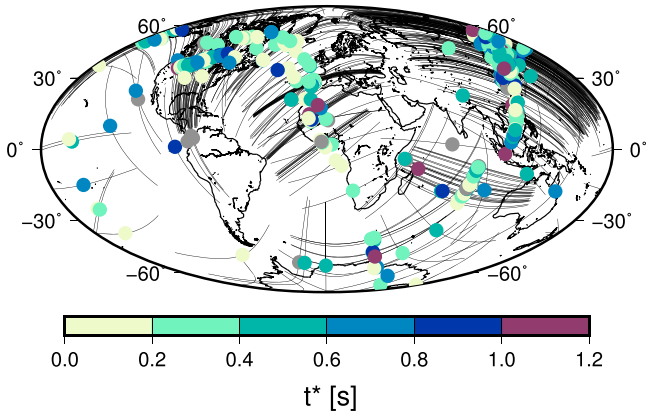

Figure 2. The t^* estimates obtained in this study using the events listed in Table 2. Black lines are portions of raypaths propagating through the inner core, and filled circles are t^* estimates plotted in the locations of the bottoming points of their respective raypaths. The range of the color scale has been adjusted to clearly show the majority of estimated t^* parameters and their variety. All estimates larger than 1.2 plot as gray filled circles (see text for explanation).

which reads as "the probability of the model **m** is true given the data **d**, is proportional to the probability of observing the data (the data is true) given the model, times the probability of the model." The second factor on the right-hand side of equation (7) is called the *prior* probability. It represents our a priori knowledge of the model, i.e., everything that we think we know about the model before observing the data. This prior knowledge is modified by the measured data through the likelihood on the right-hand side of equation (7). These two factors together combine into a *posterior* probability, the factor on the left-hand side of equation (7), which represents our a posteriori knowledge of the model in the light of the measured data.

We make simplifications for the likelihood function and assume that our measurements are independent and that our knowledge about one data point has no influence on the prediction of another. If we also assume that the noise (errors) associated with these measurements can be reasonably represented as an uncorrelated Gaussian process, then the probability of one individual measurement d_j can be written as

$$P\left(d_j|\mathbf{m}\right) = \frac{1}{\sigma_j\sqrt{2\pi}} \exp\left[-\frac{\left(p_j - d_j\right)^2}{2\sigma_j^2}\right], \tag{8}$$

where p_j is the prediction of jth datum and σ_j is the error of datum d_j.

The prior $P(\mathbf{m})$ is a Gaussian distribution with mean $\mathbf{m}_p$ and standard deviation $\frac{1}{\alpha}$. The vector $\mathbf{m}_p$ in this case is a reasonable, expected value of our parameters given by $\mathbf{m}_p = \ln(\mathbf{Q_p}^{-1}{}_p)$, where, as we will see later, $\mathbf{Q_p}_p$ is a fixed vector of reference Q_p value for the inner core. With this definition we write the prior probability as

$$P(\mathbf{m}) = \left(\frac{2\pi}{\alpha^2}\right)^{-\frac{N}{2}} \exp\left[-\frac{\alpha^2}{2}\left|\left|\mathbf{m} - \mathbf{m_p}\right|\right|_2^2\right], \tag{9}$$

where N is the number of parameters.

Since we assumed a Gaussian prior, by substituting equations (8) and (9) into equation (7) and assuming a standard deviation σ for each datum, we can express the logarithm of the posterior probability density function (PDF) as

$$L = \ln\left(P\left(\mathbf{m}|\mathbf{d}\right)\right) = \ln A - \frac{1}{2}\left[\left|\left|\frac{\mathbf{Gm} - \mathbf{d}}{\sigma}\right|\right|_2^2 + \alpha^2\left|\left|\mathbf{m} - \mathbf{m_p}\right|\right|_2^2\right], \tag{10}$$

where

$$A = \left(2\pi\sigma^2\right)^{-\frac{D}{2}} \cdot \left(\frac{2\pi}{\alpha^2}\right)^{-\frac{N}{2}} \tag{11}$$

is the scaling factor, D is the number of data, and N is the number of parameters. The maximum of the posterior will obviously occur when the factor in square brackets is minimum. The optimal solution **m** is therefore called

the least squares solution. To obtain the most probable estimate of the model **m**, we inspect the behavior of the posterior PDF around its maximum by differentiating it with respect to the model vector **m** and expanding it into a Taylor series around the maximum $\mathbf{m}^*$. Keeping only the terms up to a quadratic order in the Taylor expansion, we can express the posterior probability density function as [see *Sivia and Skilling*, 2006]

$$P(\mathbf{m}|\mathbf{d}) \propto \exp\left[\frac{1}{2}\left(\mathbf{m}-\mathbf{m}^*\right)^T \nabla\nabla L\left(\mathbf{m}^*\right)\left(\mathbf{m}-\mathbf{m}^*\right)\right], \tag{12}$$

where L is the logarithm of the posterior PDF defined by equation (10). The multivariate Gaussian in equation (12) has a maximum given by the vector $\mathbf{m}^*$. $\nabla\nabla L$ is the symmetric $N \times N$ matrix of second derivatives (i.e., the Hessian) of the posterior PDF with respect to N model parameters. The spread of the posterior distribution is related to the inverse of the second-derivative matrix:

$$\sigma_{mij}^2 = -\left[(\nabla\nabla L)^{-1}\right]_{ij}. \tag{13}$$

The $\sigma_{\mathbf{m}ij}^2$ defines the elements of the model covariance matrix. From it, we can compute the model correlation matrix by rescaling

$$\mathrm{Corr}_{ij} = \frac{\sigma_{mij}^2}{\sigma_{mii}\sigma_{mjj}}. \tag{14}$$

With the above assumptions in place we can represent any given t^* measurement in the form of equation (8). As we have just shown, this allows us to solve the problem in the least squares sense and using Bayesian inference. Since we assumed that our measurements are independent and the noise on the data is caused by a Gaussian process, our inversion parameters — the natural logarithm of inverse Q_p — are normally distributed as a consequence. It is straightforward to show, using principles of error propagation, that if the logarithm of a random variable X is normally distributed with mean μ and standard deviation σ, then the inverse of variable X is lognormally distributed with location parameter $-\mu$ and spread σ. The lognormal PDF is given by

$$P = \frac{1}{X\sigma\sqrt{2\pi}} \exp\left[-\frac{(\ln X - \mu)^2}{2\sigma^2}\right], \quad X \in (0, +\infty). \tag{15}$$

The inversion solution will be μ_i for each of the N normally distributed parameters, and the diagonal of the model covariance matrix, computed using the Hessian (equation (13)), will provide $\sigma_{\mathbf{m}i}$ for each of the normally distributed parameters. Variable X here relates to our ${Q_p}^{-1}$. Our Q_p model is then obtained with direct conversion $Q_{p_i} = \exp(-\mu_i)$, and the confidence intervals (used to plot the uncertainty maps) are computed using the cumulative distribution function of the lognormal distribution and evaluating where it is equal to $1\sigma \approx 68\%$. Note that this direct conversion to Q_{p_i} is the median of the lognormal distribution by definition. This is why in all our results we are reporting the values of the median of the lognormal distribution and plotting the full distributions to show their shapes and the effect thereof on the uncertainties.

3.2. Regularization

Without explicitly knowing the standard deviation σ of the data used in equation (10), there are many solutions that can fit the data equally well in the least squares sense. In order to stabilize the solution, we turn to two methods of regularization. As shown in section 3.1 the maximum of the PDF occurs when the expression

$$\left|\left|\frac{\mathbf{Gm}-\mathbf{d}}{\sigma}\right|\right|_2^2 + \alpha^2\left|\left|\mathbf{m}-\mathbf{m_p}\right|\right|_2^2 \tag{16}$$

is minimum. **G** is the kernel matrix relating the data **d** and the model **m**, and α^{-1} is the standard deviation of the Gaussian prior and the regularization parameter. The terms in equation (16) are the norm of the misfit between the data and the model, and the model norm multiplied by the regularization factor α^2, respectively. We will refer to these two terms as the χ^2 misfit and the damping norm. Note that the damping norm does not contain the factor α^2. In Bayesian terminology we can view these two terms as the likelihood function and the prior, respectively. As we increase α we add more weight to the model norm, or the prior $\mathbf{m_p}$, and we are penalizing models that deviate significantly from our prior knowledge. On the other hand, decreasing α will add more weight to the misfit, or the likelihood function, and the information from the data controls the inference more than the prior knowledge. Fixing σ (in our case to a value of 1) and tracing a curve of the model norm with respect to the data misfit for different values of the parameter α produces a characteristically L-shaped curve, known as the L curve [*Hansen*, 1992]. The corner of the curve, if it exists, defines the value of α which corresponds to a reasonable balance between the data misfit and the variance of the model.

Table 3. A Summary of Regularization and Inversion Techniques Used in This Study[a]

Label	Description
1	Using the L curve and damping parameter
2	Using discrepancy principle and damping parameter
3	Using the L curve and smoothing parameter
4	Using discrepancy principle and smoothing parameter

[a]For details on the L curve and the discrepancy principle, and on the different regularization parameters, the reader is referred to the text and chapter 5 of *Aster et al.* [2005].

Second, after obtaining the solution using the L curve, we compute the standard deviation of the residuals between the data and the model predictions, and we use this value as an estimation of noise σ in the data. We then use the discrepancy principle [*Aster et al.*, 2005] to find the best solution. In this case we assume that the uncertainties on the data are due to a zero-mean, Gaussian process that is independent in all of the observations and σ_j are standard deviations of these observations. In this Gaussian model the expected value of the misfit (first term of equation (16)) is the number of data D and corresponds to the RMS misfit of 1. The discrepancy principle dictates that the regularization parameter α must be chosen in such a way that the χ^2 misfit is as close as possible to the number of data D. To obtain the solution, μ_i, we optimize and use Newton's continuous gradient method to find the global minimum of the expression (16).

Table 3 summarizes different approaches we are using to solve the problem and different regularization techniques, i.e., damping and smoothing (see Appendix A).

4. Synthetic Tests

We performed multiple synthetic tests using our inversion algorithm. We used the checkerboard model as input. We tested the inversion with different guesses for the initial model supplied to the optimization algorithm. We also experimented with different amounts of Gaussian, uncorrelated noise of 2%, 5%, and 10% added to the synthetic data. In this way we confirmed that adding 2% of the range of synthetic data is a reasonable amount of noise, while with 5% and 10% noise the recovery was poor or impossible. Experiments also showed that the inversion will converge to virtually indistinguishable answers no matter the starting guess.

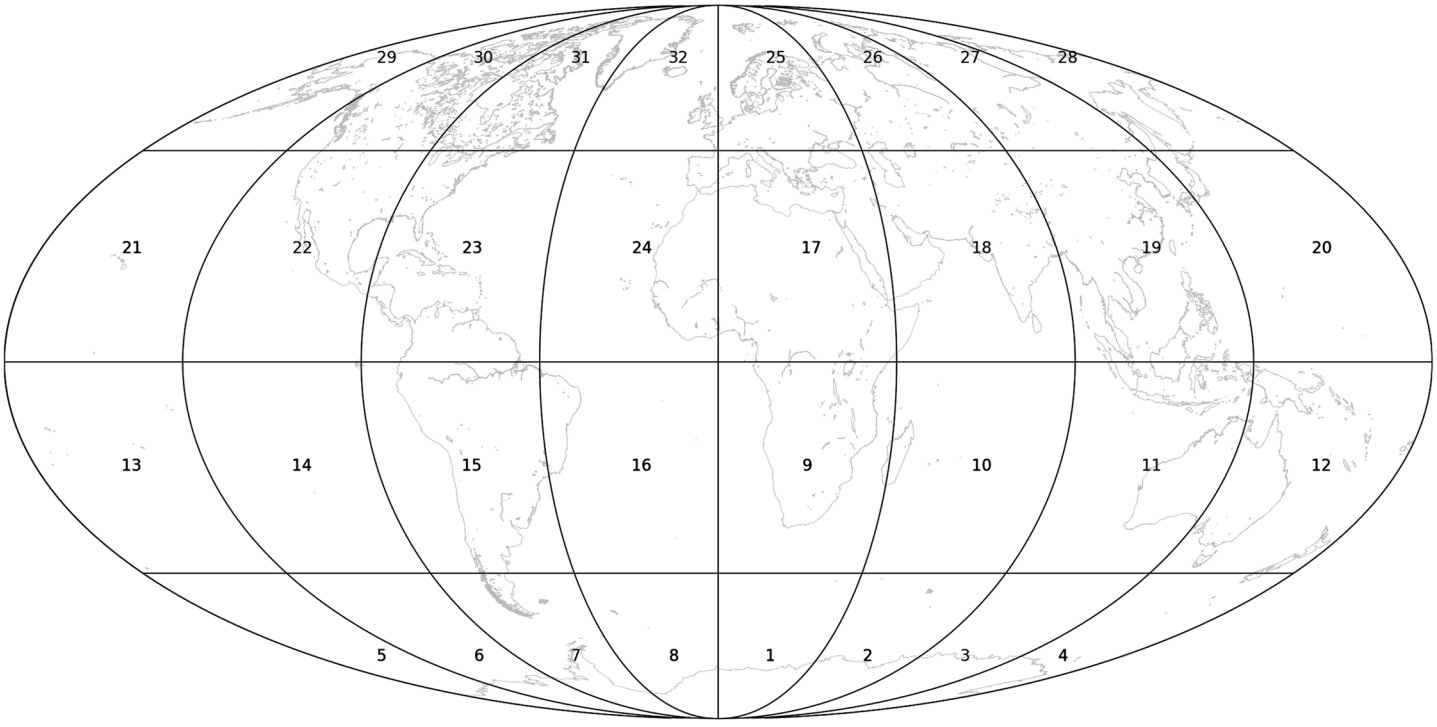

Figure 3. Locations of model parameters in block parameterization and their indices.

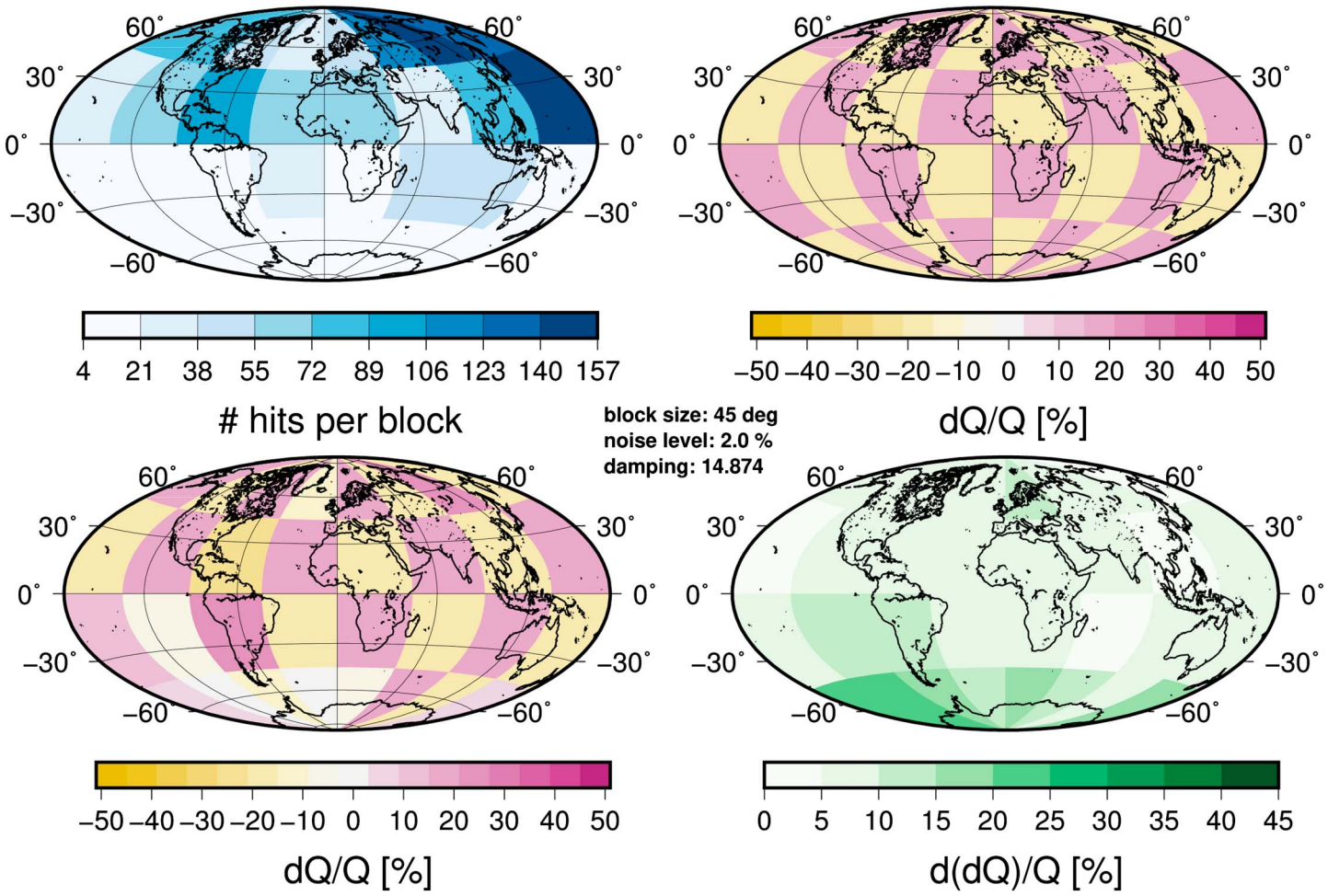

Figure 4. Synthetic tests. (top left) The number of ray hits for each parameter block. The image reflects Figure 2 with high number of hits in areas of dense coverage. (top right) The input model for this particular synthetic test. It is a checkerboard model of alternating blocks with Q_p of 200 and 300. These values are shown as deviations from a model average ($Q_p = 250$). (bottom left) An inversion recovery of the checkerboard model using the discrepancy principle. (bottom right) The uncertainties on the recovered model. In this case only the values here are confidence intervals of 3σ. The values are expressed as percentages of the recovered model.

If, for whatever reason, this guess is not good enough, the algorithm will not converge. We settled with the initial guess being a constant vector of $Q_p = 250$ for both synthetic tests and later for the real data inversion. Below we present synthetic tests and results for 45° sized block parameterization of the inner core. The blocks are 45° long and wide, and they encompass one thick layer of the upper inner core down to 400 km below the inner core boundary. These blocks, i.e., model parameters, are numbered and located as shown in Figure 3.

We do not attempt to resolve depth changes of attenuation. We have also tried performing inversion with the 30° sized blocks, and while the recovery of the input model looks relatively good, the underlying uncertainties seem to indicate that we do not have the required resolution for this parameterization.

In both synthetic test and the real data inversion the prior was fixed to a constant Q_p of 300. This is the value most commonly reported on, as discussed above and seen in Table 1; we take it as a reasonable prior expectation of the Q_p factor within the inner core. This being our prior, we penalize all the models that deviate significantly from that value. The synthetic tests were performed using the approach described above, utilizing the discrepancy principle. Since all the parameters in the synthetic tests are known, including the noise added to synthetic data, there was no need to perform the L curve test. One example of the synthetic test is shown in Figure 4. The upper left corner of this figure shows how many times each of the blocks has been hit by a seismic ray. It is a reflection of Figure 2 showing a large number of hits where the ray coverage is dense and a low number of hits where the coverage is poor. Figure 4 (top right) shows the input model for this synthetic test. It is a checkerboard model with alternating Q_p factor of 200 and 300. The alternating

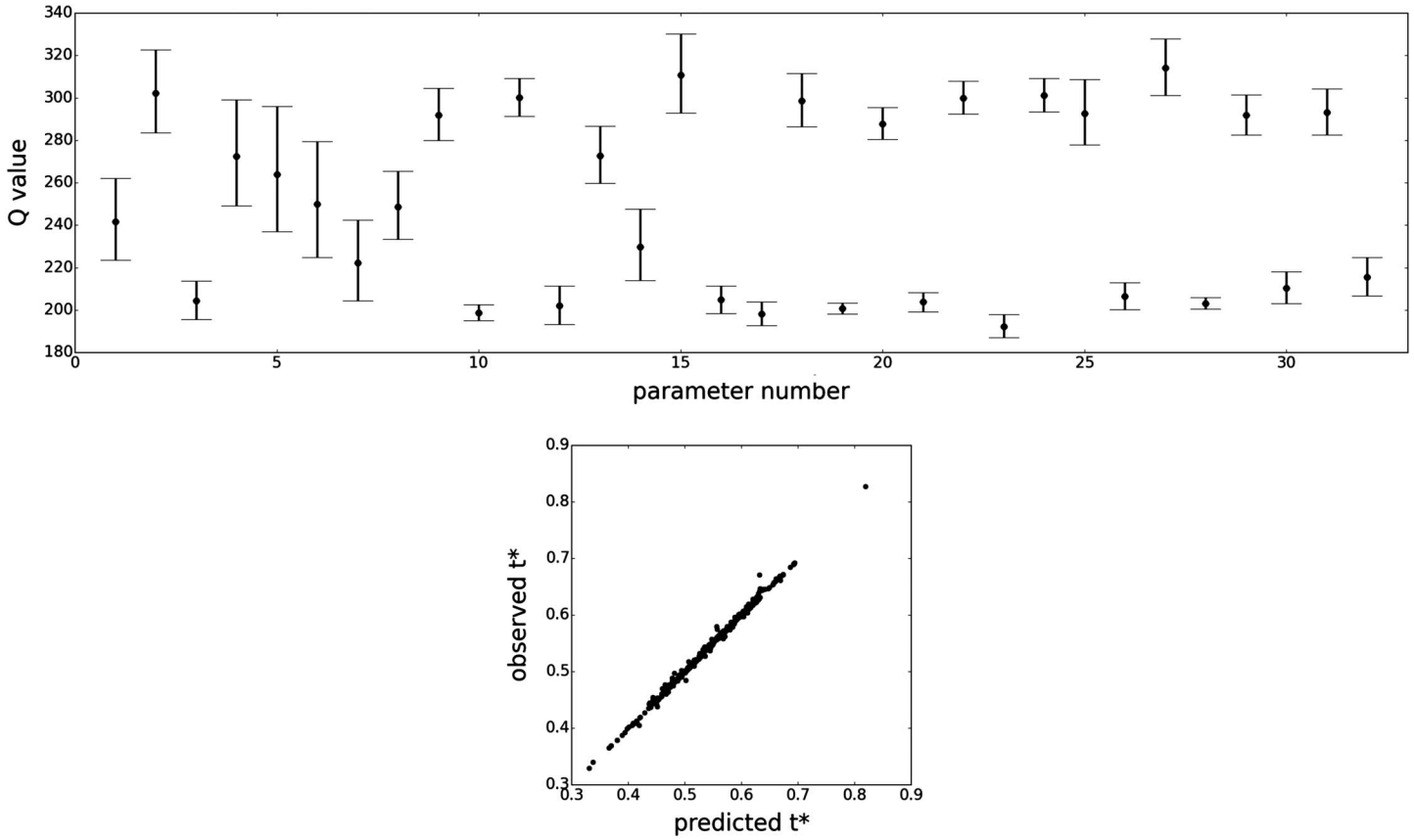

Figure 5. (top) The recovered model in a synthetic test (black filled circles) and its 3σ confidence interval (error bars). Parameters are numbered as shown in Figure 3. We can see larger uncertainty for the first 10 parameters, which are all in the Southern Hemisphere. (bottom) The relationship between observed and predicted data shows good recovery of the input model.

checkerboards are shown here as a deviation from the input model average ($Q_p = 250$). Figure 4 (bottom left) shows the recovery of the input model (with added 2% noise) using the methods described above and the discrepancy principle. We see that the recovery is reasonably good everywhere except in the Southern Hemisphere, particularly below 45° south latitude. Obviously, the coverage is very poor mostly in the Southern Hemisphere, and this will be reflected in the resulting model and its uncertainties. The uncertainties in that region are therefore higher than in any other region, as shown in the lower right corner of the figure. The uncertainties are confidence intervals of 3σ (in the case of synthetic tests only!) and expressed as percentages of the recovered model. Also displayed in the figure is the optimal damping parameter for this particular case obtained using the discrepancy principle.

The predicted model parameters and their 3σ confidence intervals are given in Figure 5 as black filled circles and error bars, respectively. The parameters (blocks) are numbered as shown in Figure 3. That is why in Figure 5 approximately the first 10 parameters have larger confidence intervals — they are located in the south of the Southern Hemisphere. Alongside this image we also show linear relationship between the observed and predicted data, with the slope of the line being 45°. This is a further testimony to good recovery of the input model.

The synthetic tests show that with the current data set and parameterization we should be able to resolve an average representation of the lateral attenuation structure of the upper inner core reasonably well.

5. Real Data

We do not know what the noise estimate is on the real data. Hence, we first obtain a noise level estimate as described in section 3.2 by computing the L curve. We run the inversion multiple times (at least 2000 times) with different damping parameters α and plot the two terms, the χ^2 misfit and the damping norm, from

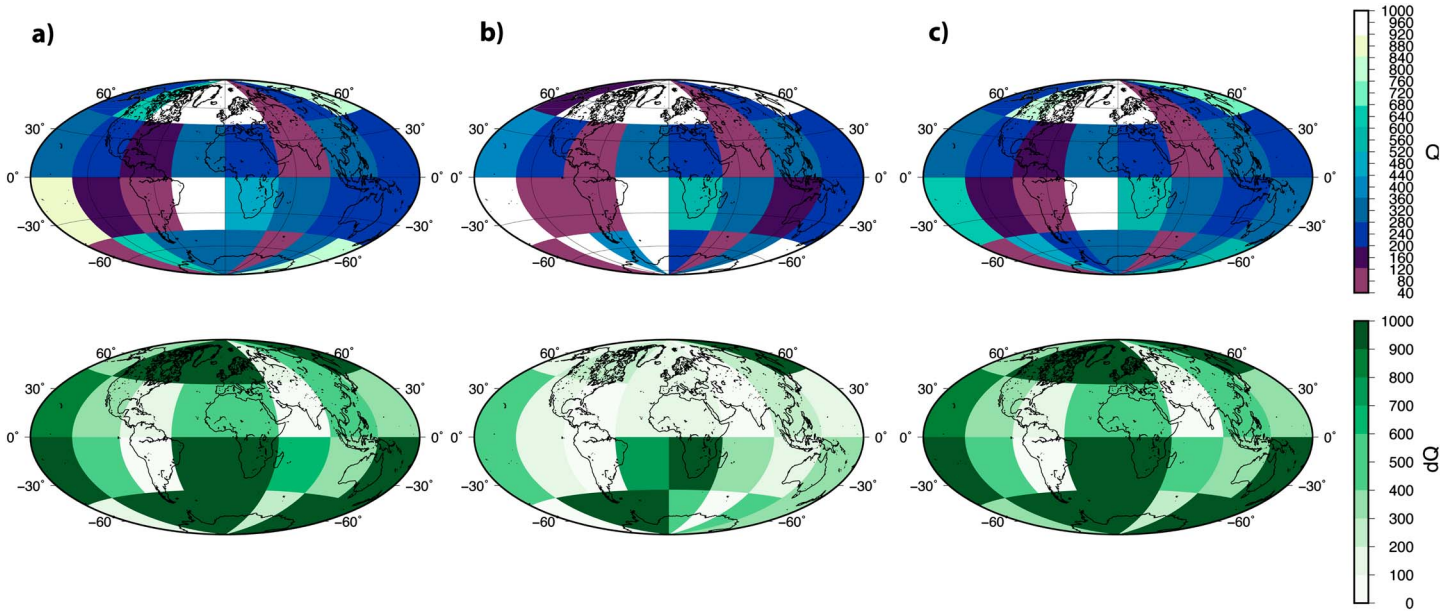

Figure 6. Inversion results using three different approaches to regularization. (top row) The optimal solutions to the inversion and (bottom row) the corresponding uncertainties of those solutions. (a) Inversion result and its corresponding 1σ confidence interval obtained using approach 1 from Table 3. (b) Same as Figure 6a but using approach 2 from Table 3. (c) Same as Figures 6a and 6b but using approach 3 from Table 3. The values shown are absolute values of Q_p.

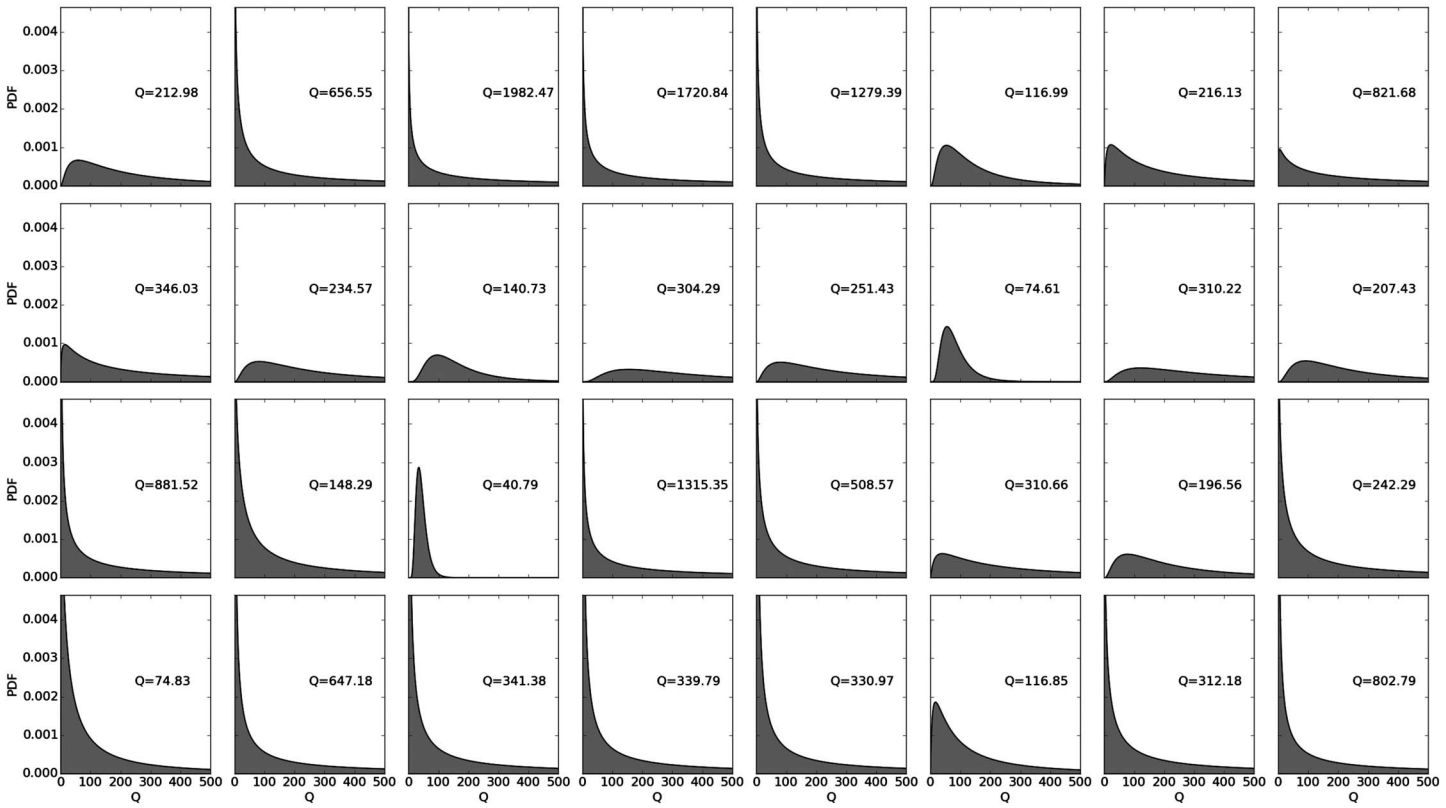

Figure 7. Theoretical lognormal distributions for each parameter of the solution shown in Figure 6a, obtained using approach 1 from Table 3. The diagrams are ordered in the same manner as the blocks of Figures 3, 6a, and 4 and are representative of the corresponding locations. For example, the bottom left diagram is representative of the block labeled 5, while the top right diagram is representative of the block labeled 28 in Figure 3. The value of Q_p in each diagram corresponds to the median of associated lognormal distribution.

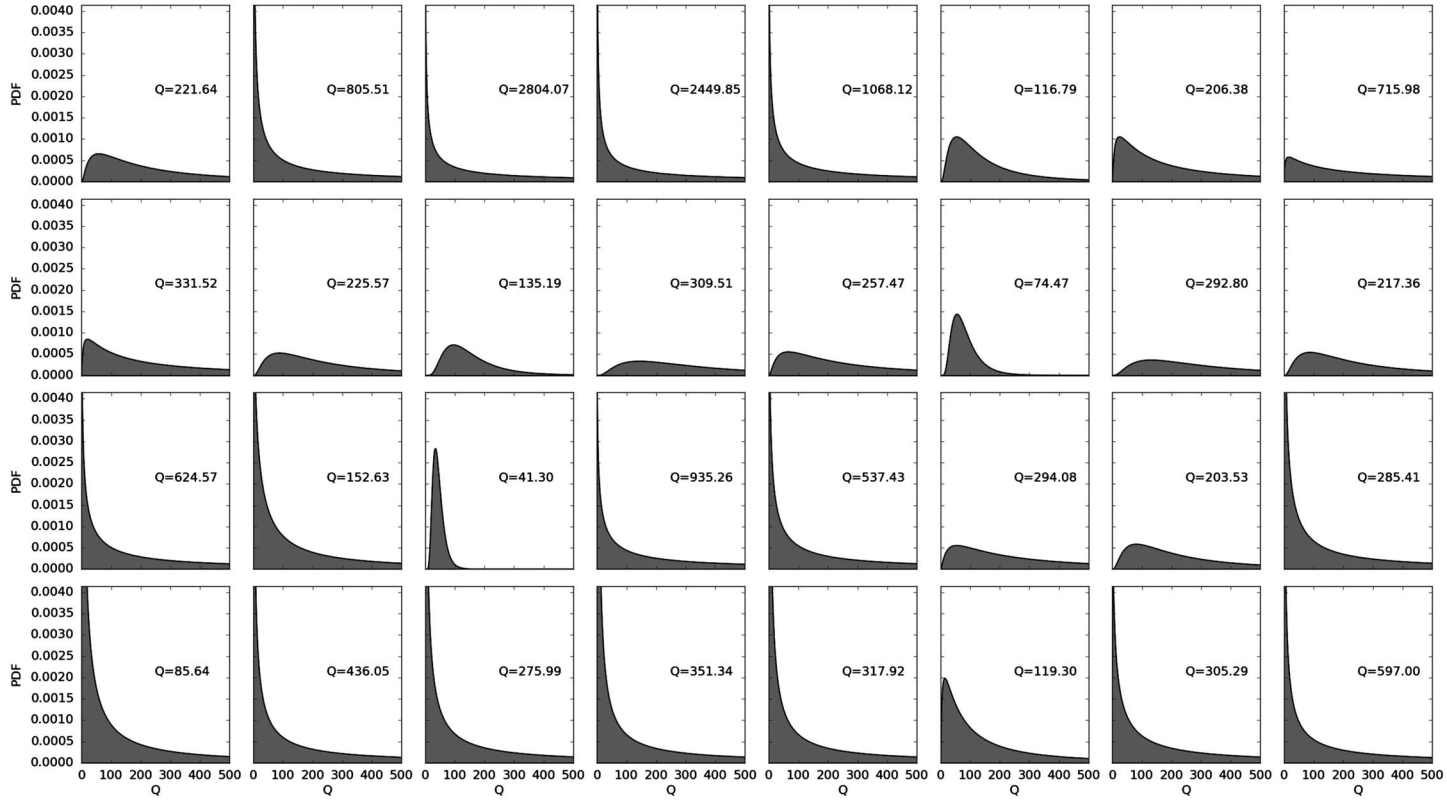

Figure 8. Same as Figure 7 but for the solution shown in Figure 6c, obtained using approach 3 from Table 3.

equation (16) one against the other for corresponding damping parameters. We then choose the damping parameter α in the vicinity of the corner of the resulting curve to run our final inversion. This is approach 1 from Table 3. Once we obtain a model in this way, we use the standard deviation of the t^* residuals as a noise estimate for the data and set the standard deviation on the diagonal of the data covariance matrix to that value; the off-diagonal elements are set to 0. Once we have this estimate of noise, we can use the discrepancy principle, and we then employ approach 2 from Table 3, run the inversion again, and compare the results. When employing approach 2, we optimize for the damping parameter α by running the inversion at least 2000 times with different damping parameters and finally choose the one for which the χ^2 misfit (first term in equation (16)) is as close as possible to the number of data. We then run our final inversion using the optimal damping parameter.

This principle is the same for approaches 3 and 4 in Table 3, the only difference is in the regularization matrix, since for approaches 3 and 4 we use smoothing rather than damping. The details of the regularization matrix are shown in Appendix A.

Figures 6a–6c shows the results of the inversion employing approaches 1–3 from Table 3, respectively. While solutions (a) and (c) are relatively stable, the optimal regularization parameter for solution (b) obtained the minimal possible value, essentially providing an undamped solution and signaling a failed discrepancy principle approach. Additional information and details on this and each of the other inversion processes for these results can be found in Appendix B. Nevertheless the acquired results are all similar, as discussed below. Figure 6 (top row) shows the resulting attenuation models, and Figure 6 (bottom row) shows the 1σ confidence intervals for the respective models. The values in this figure are all absolute values of Q_p. The color scales for the result and the uncertainties are the same for all three approaches and are saturated for their maximum value, so all the values larger than the maximum on the color bars are shown in the color of the maximum value.

The three sets of results in Figure 6 show similar patterns. We observe high attenuation with Q_p between 200 and 300 beneath the western, central, and northern Africa and central Atlantic and down to 75 beneath India. High attenuation occurs beneath Southeast Asia with Q_p between 200 and 300. This high attenuation

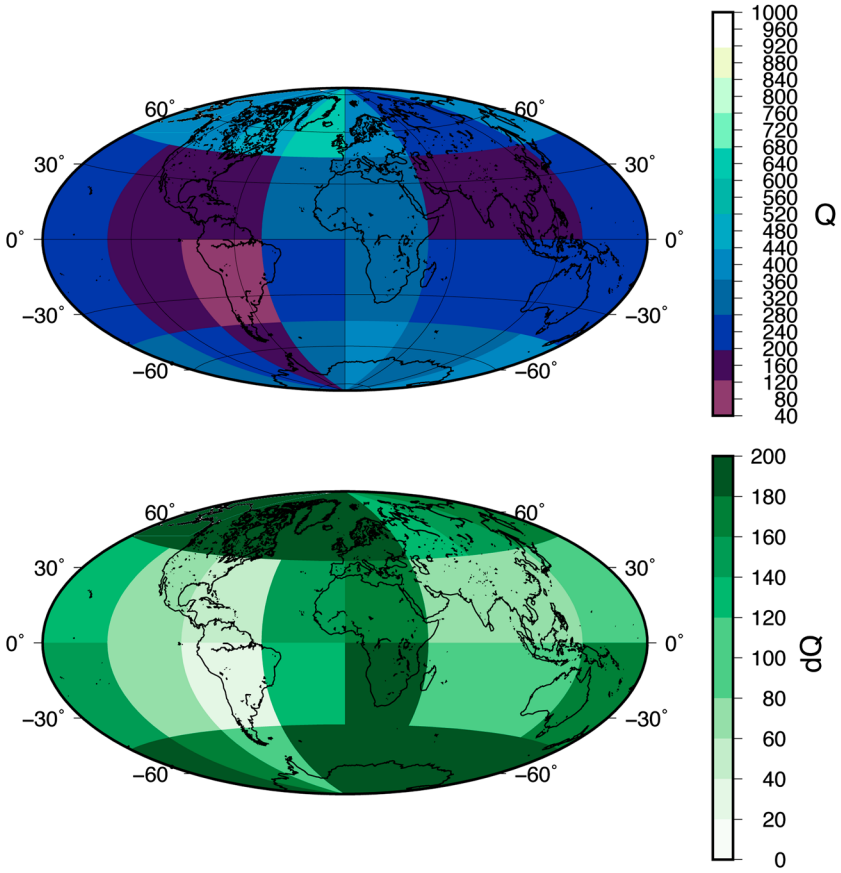

Figure 9. Preferred tomographic model of Q values obtained for the 400 km thick layer at the top of the inner core. (top) The smooth solution of the inversion. The inversion was performed using approach 4 (see Table 3). (bottom) The 1σ confidence intervals for each parameter block; note that the uncertainty scale here is compressed relative to the one in Figure 6. Shown in these images are the absolute values of estimated Q_p and their confidence intervals.

extends through entire Pacific all the way through to central America, with Q_p values ranging between 140 and 345. We see high attenuation around the Indian Ocean and Australia with Q_p values between 200 and 300. Low attenuation patches occur beneath north Atlantic and the eastern part of Canada. Because of the poor coverage in southern regions and especially around South America, we will not interpret the attenuation model in regions south of 45° south latitude and regions beneath the continent of South America and parts of Pacific west of it.

The confidence intervals here are associated with the lognormal distribution, and the final result for the Q_p model cannot therefore be represented as $X \pm X_\sigma$, where X and X_σ represent the mean and standard deviation of a Gaussian distribution, respectively, as the lognormal distribution is an asymmetric distribution. To get a better estimate of this confidence interval and what it actually means for the results, we used the normally distributed parameter estimates directly from the inversion and the diagonal terms of the model covariance matrix (shown in Appendix B) to construct a lognormal distribution for each parameter. Lognormal probability distributions for results shown in Figures 6a and 6c are shown in Figures 7 and 8, respectively. Due to the instability of solution (b), numerical computation of the lognormal distributions of its parameters failed and hence these distributions are not shown. Each small diagram in Figures 7 and 8 represents a probability distribution function for each Q_p parameter. The order of the diagrams corresponds to the block locations as shown in Figure 3 and the maps in Figure 6. The lower left diagram hence represents the lower left block, labeled with number 5 in Figure 3, and the entire fourth row of diagrams represents the southernmost row on the map. The upper right diagram represents the block labeled 28 in Figure 3. From these figures it is again obvious that the blocks in the Southern Hemisphere are poorly resolved. All the diagrams in the last two rows of Figures 7 and 8 show very wide distributions, slowly approaching 0. Conversely, the blocks in the regions with better coverage are much better resolved showing narrower probability distributions. Some of them are still

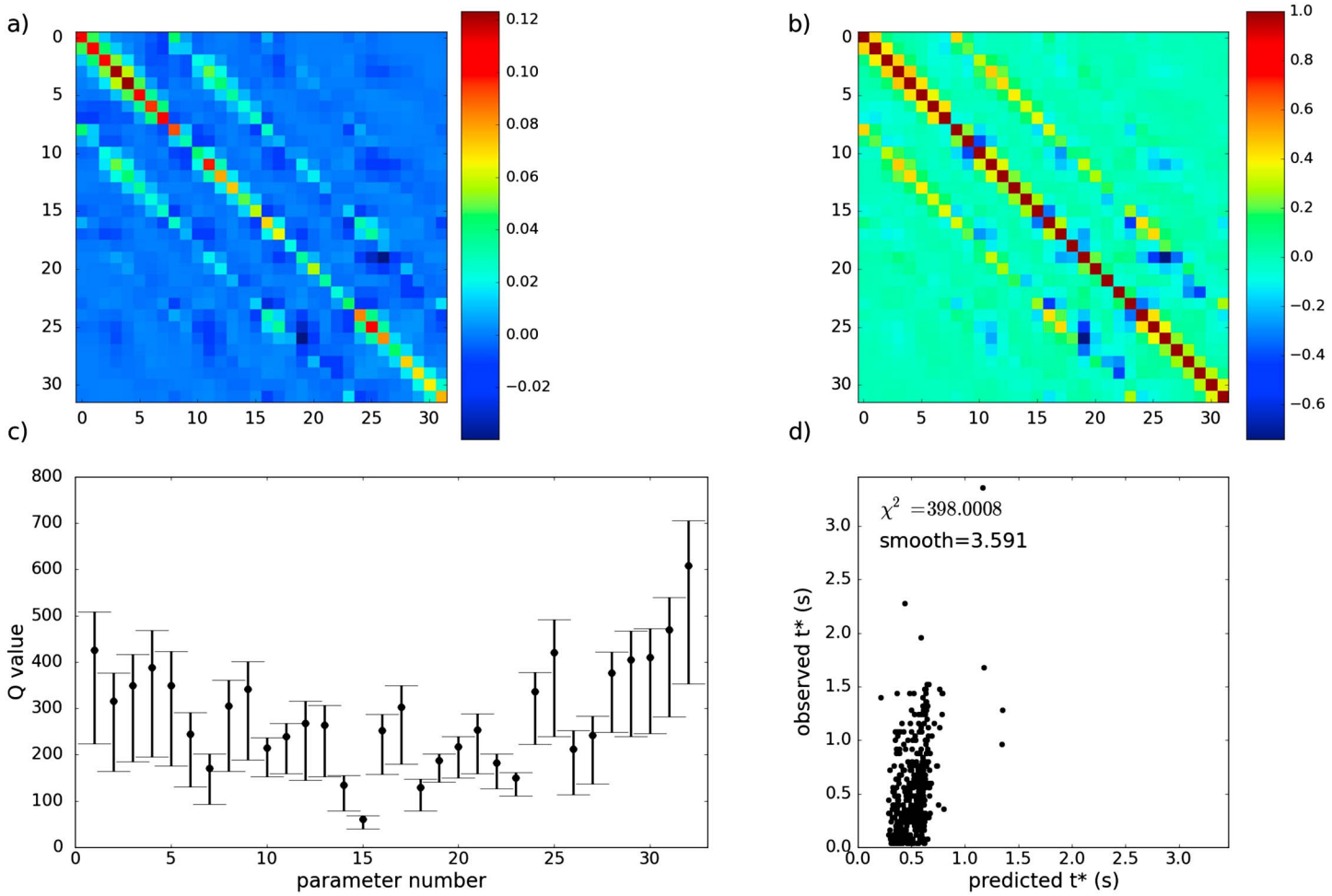

Figure 10. Inversion statistics corresponding to the results shown in Figure 9. (a) Model covariance matrix for parameters $\ln(Q_{p_i})$. (b) Model correlation matrix computed directly from Figure 10a. (c) The recovered Q_p model (black filled circles) and its 1σ confidence interval (error bars). (d) Observed data plotted as a function of predicted data. Also shown are the selected smoothing parameter of 3.591 and the χ^2 misfit between the observations and predictions. Since this particular inversion was performed using the discrepancy principle, the χ^2 misfit here is a diagnostic of a successfully chosen regularization parameter as it is equal to the total number of observed data (398).

quite wide or they have a small peak, pointing to a larger uncertainty and a poorer estimate. The values of Q_p given in each little diagram correspond to the median of the associated lognormal distribution as discussed in section 3.1.

Finally, we performed the inversion using approach 4. The standard deviation of the residuals, which we used as a noise estimate, in this case was 0.38. Using that value for noise to perform the inversion using the discrepancy principle resulted in a smooth image with a large number of blocks having the value of Q_p close to 300. While a smooth image is what one would expect running an inversion using smoothing as a mean of regularization, this value is obviously close to our imposed prior. To check whether this is the right solution, we changed the prior to $Q_p = 700$ and ran the inversion again with the same value for data noise (0.38). The algorithm converged to similar (and indistinguishable) solution, and this is our best solution shown in Figure 9. This image is somewhat different from the ones in Figure 6. As expected, it is much smoother and this effect is visible the most in the southern regions where coverage is poor. The confidence intervals are much smaller here too, as can be seen from the uncertainty map in the bottom row of Figure 9, from Figure 10c where they are plotted as error bars on the optimal model (black filled circles), and from the lognormal distributions for the parameters shown in Figure 11. It is not surprising though that both covariance and correlation matrix in Figures 10a and 10b show correlation between more parameters than we saw previously, since we are essentially requesting that the parameters be as similar as possible by using smoothing. The most interesting feature of this solution for approach 4, shown in Figures 9–11, is the consistency with the solutions shown

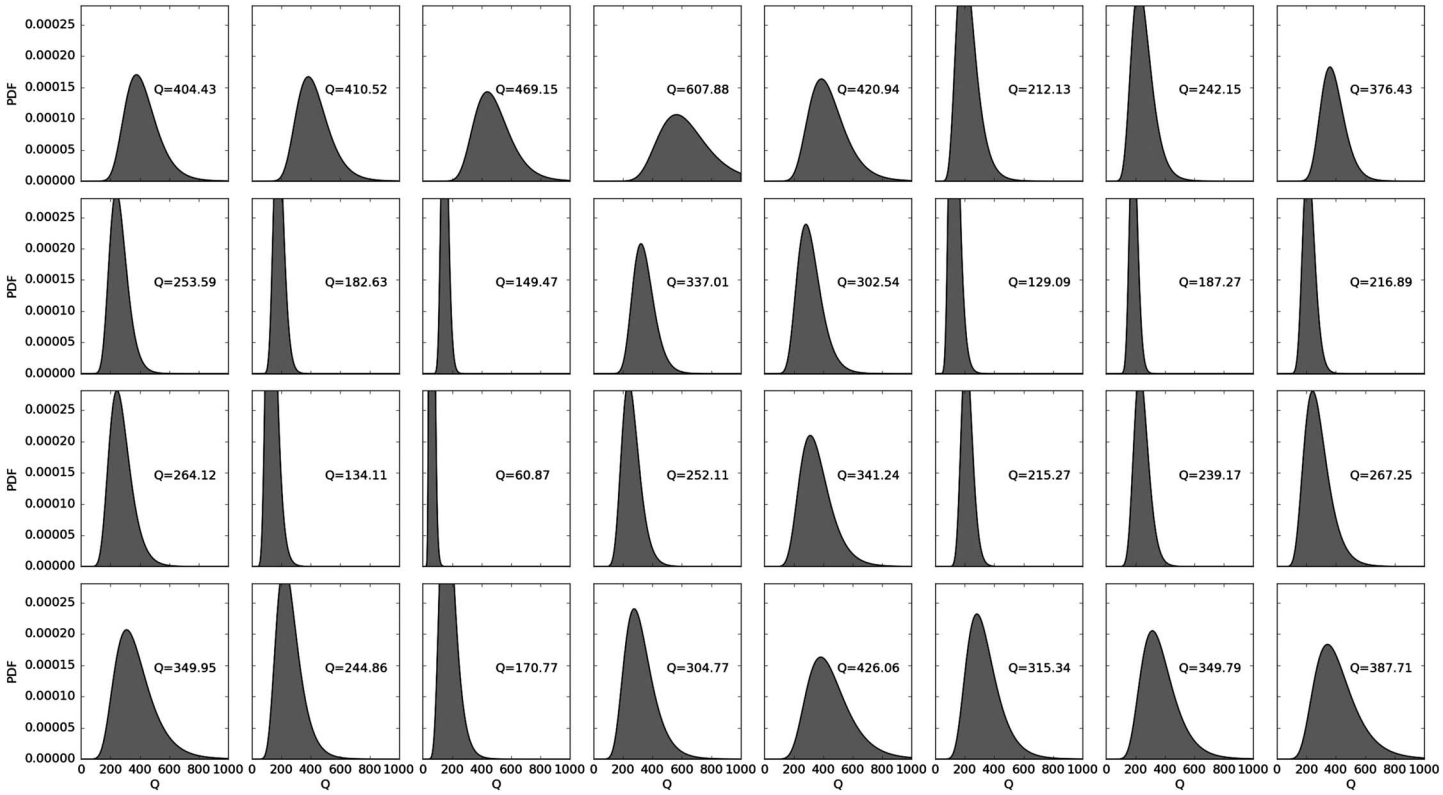

Figure 11. Theoretical lognormal distributions for each parameter of the solution shown in Figure 9. The diagrams are ordered in the same manner as the blocks of Figures 3, 9, and 4, and are representative of the corresponding locations. For example, the bottom left diagram is representative of the block labeled 5, while the top right diagram is representative of the block labeled 28 in Figure 3. Smoothing regularization forces parameters to be similar resulting in relatively narrow distributions for the southernmost parameters. The value of Q_p in each diagram corresponds to the median of associated lognormal distribution.

in Figure 6, specifically for the areas around Africa, central and Southeast Asia, Pacific, Indian Ocean, and Australia. The reader should note a different scale for Q_p uncertainties in this result. We observe high attenuation beneath Africa and Middle East with Q_p between ≈130 and ≈340 and high attenuation beneath Southeast Asia, Indian Ocean, and Australia with Q_p between ≈187 and ≈270. High attenuation spreads throughout the Pacific and beneath North America with Q_p ranging between 150 and 250. Low attenuation occurs beneath the North Atlantic.

5.1. Observed High Attenuation Beneath South America and India

We are aware of extremely high attenuation that occurs beneath South America and India in our results, with Q_p on the order of 40 and 70, respectively. These are two of the best resolved blocks (of the lowest uncertainty) in our inversion, and it is tempting to interpret them in that light; however, we would like to warn the reader against this. While the block covering India has a decent amount of ray hits, it is still in the area with a relatively poor coverage. The rays passing through that block are just touching on it around its edges. It so happens that these rays cross each other, coming from different azimuths, and this constrains the result for that block better because the equations governing it will be linearly independent. This is definitely influencing the low confidence interval for this block.

The block beneath South America has exactly four hits by seismic rays, and those are on the corners of the block. It is obvious from Figure 2 that there is no coverage in that region, and hence the obtained result should not be interpreted. The rays that are touching on this block are also coming from different azimuths and constraining the numerical result well, but this result is not representative of the region.

Simultaneously, the results shown in Figures 6a and 6b are damped solutions to the problem. It is well known that when damping is applied to the model, all the parameters are equally damped, and it is possible that we see this effect in the blocks in question. It should be noted that in our last solution, shown in Figure 9, which

we consider the best solution to this problem, the value of Q_p beneath India shifted toward ≈130, while the one beneath South America has not changed much—unsurprisingly due to the poor coverage.

6. Discussion

We performed the inversion for one thick layer, spanning ≈400 km of the inner core below the ICB, using global data of 398 t^* measurements from 50 events. The results show fairly high attenuation beneath Southeast Asia, Indian Ocean, and around Australia, with this patch extending through the entire Pacific all the way to the Americas. Patches of low attenuation are observed beneath north Atlantic, Africa, and northeastern parts of North America.

Earlier study by *Wen and Niu* [2002] revealed a hemispherical pattern in attenuation of the uppermost inner core (top ≈85 km). According to that study, a possible scenario that explains this dichotomy involves different fractions of melt inclusions in the inner core, as described by *Singh et al.* [2002]. Better connected liquid inclusions result in higher porosity and hence lower seismic velocities and attenuation, while well-isolated inclusions result in lower porosity, higher velocities, and higher attenuation dominated by scattering effects. If at the same time higher porosity is indicative of faster crystallization, then, explaining seismic observations, this scenario implies that the quasi-Western Hemisphere of the inner core is colder than the quasi-Eastern Hemisphere. To support this entire mechanism, a vigorous translational convection in the inner core is required, driven by the thermal anomalies at the bottom of the outer core. This type of mechanism is a feature of models by *Monnereau et al.* [2010] and *Alboussière et al.* [2010]. According to *Deguen et al.* [2013], if the inner core is unstably stratified, the translation mode dominates only if the viscosity is large enough, with a critical value on the order of $3 \cdot 10^{18}$ Pa s. This depends on the convection in the outer core and its potential to supply or remove the latent heat of melting or solidification. If the viscosity is small, the convection forms in axisymmetric mode at the onset and plume convection at large Rayleigh number. With viscosity being poorly known, either of these scenarios is possible.

Nothing about our results suggests the hemispherical dichotomy of the inner core for this layer; however, the results are in line with findings of *Attanayake et al.* [2014] and *Iritani et al.* [2014a, 2014b]. Note that *Attanayake et al.* [2014] also used 45° wide bins in their study. Our results are specifically in agreement with Figure 4 of *Iritani et al.* [2014b], when one takes into account the depth extent of our data set, which approximately covers the middle third of the depth extent of their models for three regions within the inner core. In all of the results shown, regardless of regularization technique, we observe relatively high attenuation throughout the belt of Pacific-Atlantic-Asia. The result shown in Figure 9 is our best result, and in it we can see high attenuation beneath Asia and the entire Pacific, stretching all the way to the Atlantic. Only beneath Atlantic and Africa we observe slightly lower attenuation than in the rest of that belt (with Q_p larger than 300 beneath Atlantic and Africa and generally lower than 300 beneath Pacific and Asia). It is possible that our parameterization of 45° sized blocks could affect the recovery of hemispheric boundaries. While finer parameterization effectively imposes more (and different) boundaries in the model, we do not have the resolution to recover the structure using a finer grid. Even coarser parameterization significantly smooths out the solution and provides a false impression of good resolution. One way to mitigate this issue with the boundaries would be to possibly shift the grid; however, we choose not to pursue it here, as we are currently using the same data set to perform transdimensional Bayesian inversion, where strict parameterization and explicit regularization are not imposed.

The geodynamical scenario that involves convection/translation cannot explain the type of pattern we observe here. Furthermore, some of the more recent works by *Pozzo et al.* [2014] and *Gomi and Hirose* [2015] report on high thermal conductivity at inner core temperatures and pressures indicating that thermal convection within the inner core is highly unlikely, as the latent heat is being efficiently transferred into the outer core via conduction.

The models of *Aubert et al.* [2008] and *Gubbins et al.* [2011], while illustrating slightly different interactions between the inner core and the lowermost mantle, both predict degree 2 heterogeneity (for a recent review, see *Tkalčić* [2015]) in velocity and attenuation, the kind that could explain the observations of *Attanayake et al.* [2014] and *Iritani et al.* [2014a, 2014b]. Our attenuation pattern is in agreement with the one shown in those studies. The uncertainties for the specific regions interpreted here are reasonable and show that the parameters covering the upper inner core beneath Asia, Pacific, and Africa are relatively well resolved. This view-shift of attenuation pattern favors the geodynamical models advocating thermal mapping of the

lowermost mantle onto the ICB and upper inner core structure. In the case of those models, higher attenuation in regions beneath Asia and Pacific is a result of faster crystallization or freezing and consequent formation of many dendrite boundaries which interact with a propagating seismic wave.

We tried splitting our data set into two layers; however, we lose resolution and the ability to recover the attenuation structure in that case, so we cannot say whether the observed pattern is dominated by shallower or deeper structures or processes in the inner core.

Future work on the attenuation of the inner core should include a more advanced Bayesian approach, where we would also invert for the number of parameters (basis functions) and the noise of the data. Bayesian trans-dimensional inversion makes this possible and thus eliminates subjective choices or need for experimenting with regularization, and we will focus on it as our next step. As seen here, coverage of the inner core for PKPbc-PKIKP data set is still relatively poor, particularly when compared to PKPab-PKIKP or PKiKP-PKIKP data sets (see *Tkalčić* [2015] for examples). Better coverage of the inner core for the depth layers studied here would provide better constraints on the parameters and include data in the regions such as, for example, South America — the very region which is completely uncovered in our own study. This can hopefully be improved in the future by installing Ocean Bottom Borehole Seismometers (OBBS) or Ocean Island Borehole Seismometers (OIBS) as advocated recently by *Tkalčić* [2015].

Appendix A: Smoothing Regularization

To obtain the smooth solution, we can rewrite the second term, the damping norm, of equation (16) in its matrix form:

$$\alpha^2 \left(\mathbf{m} - \mathbf{m_p}\right)^T \mathbf{L}^T\mathbf{L} \left(\mathbf{m} - \mathbf{m_p}\right). \tag{A1}$$

In the case of damped solution the **L** matrix in the damping norm is $N \times N$ identity matrix, where N is the number of parameters. Damping is then applied equally to all the parameters by multiplying this identity matrix with a scalar damping parameter α.

To obtain a smooth solution, we use a 2-D Laplacian operator, ∇^2, and apply it to every parameter. The **L** matrix is in that case no longer an identity matrix but rather takes the following form:

$$\begin{bmatrix} -1.0 & 0.25 & 0 & 0 & \cdots & 0 & 0 & 0 \\ 0.25 & -1.0 & 0.25 & 0 & 0 & \cdots & 0 & 0 \\ 0 & 0.25 & -1.0 & 0.25 & 0 & \cdots & 0 & 0 \\ \vdots & & & \cdots & & & & \vdots \\ 0 & 0 & 0 & \cdots & 0.25 & -1.0 & 0.25 & 0 \\ 0 & 0 & 0 & \cdots & 0 & 0.25 & -1.0 & 0.25 \\ 0 & 0 & 0 & \cdots & 0 & 0 & 0.25 & -1.0 \end{bmatrix} \tag{A2}$$

with N rows and N columns.

In terms of Bayesian inference this is essentially posing a slightly different prior: any model that is "rough," i.e., its neighboring cells show significant deviation from each other, is penalized. With larger smoothing parameter, values between adjacent blocks will be more similar, and with increasing smoothing parameter, they will approach the value of our imposed prior. The resulting models will be smooth but not necessarily of minimum variance, as unsampled blocks will be interpolated between nearby cells. We use exactly the same procedure as before to obtain the results and regularize using the L curve first and then the discrepancy principle.

Appendix B: Additional Information on the Results

B1. Solution in Figure 6a

This solution was obtained using approach 1 from Table 3, with the damping parameter $\alpha = 0.17$ chosen from the L curve. The L curve is shown in Figure B1. This L curve was computed performing the inversion for a range of 2000 regularization parameters, and every eightieth parameter is plotted at its respective point along the curve to avoid cluttering.

Figure B2 shows the model covariance matrix (in log space), model correlation matrix, resulting model with 1σ confidence intervals, and predictions from the model fit to the observations going from left to right and top

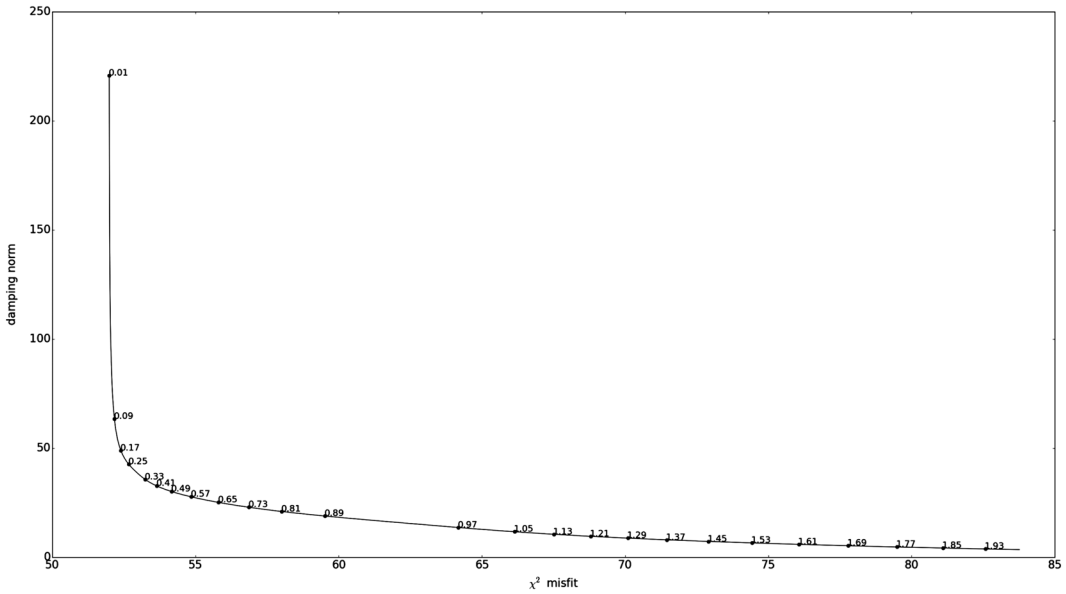

Figure B1. An example L curve computed from attenuation data in this study. Numbers along the curve correspond to the regularization parameter α used to compute that particular point on the curve. In this case the inversion was performed for a range of 2000 regularization parameters, and only every eightieth parameter is plotted along the curve.

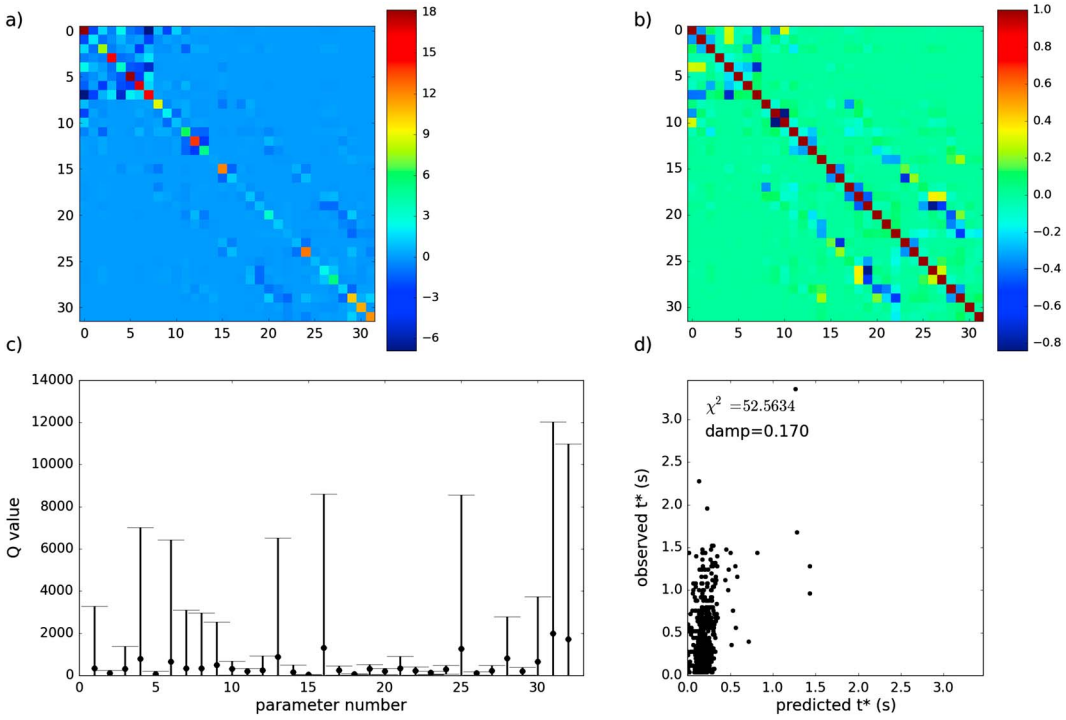

Figure B2. Inversion statistics corresponding to results from Figure 6a. (a) Model covariance matrix for parameters $\ln(Q_{p_i})$ shows high covariance between the 10–12 first parameters. All of these parameters are in the Southern Hemisphere where the ray coverage is poor. (b) Model correlation matrix computed directly from Figure B2a. It shows significant correlation between the first 10–12 parameters all located in the Southern Hemisphere but also for some of the parameters in the Northern Hemisphere. (c) The recovered Q_p model (black filled circles) and its 1σ confidence interval (error bars). (d) Observed data plotted as a function of predicted data. Also shown are the selected damping parameter of 0.17 and the χ^2 misfit between the observations and predictions.

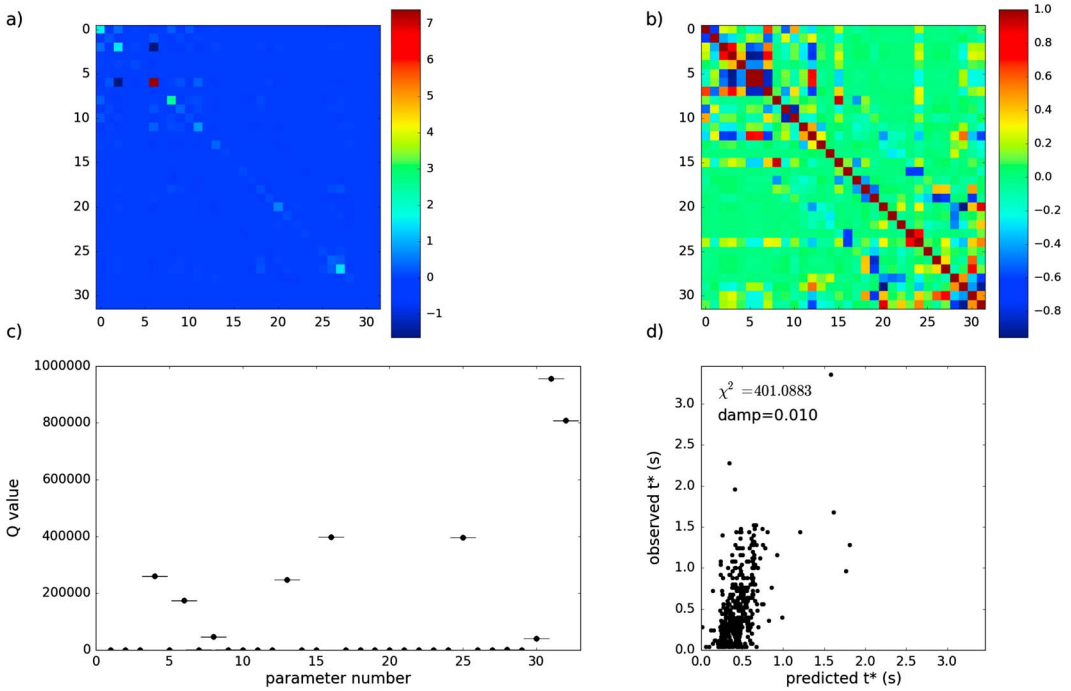

Figure B3. Inversion statistics corresponding to results from Figure 6b. (a) Model covariance matrix for parameters $\ln(Q_{p_i})$. (b) Model correlation matrix computed directly from Figure B3a. It shows significant correlation between the first 10–12 parameters all located in the Southern Hemisphere but also for some of the parameters in the Northern Hemisphere. High correlation is visible for parameters neighboring parameter number 30. (c) The recovered Q_p model (black filled circles). The 1σ confidence intervals are not visible in this plot, as they are relatively small compared to the value of recovered parameters. (d) Observed data plotted as a function of predicted data. Also shown are the selected damping parameter of 0.01 and the χ^2 misfit between the observations and predictions. Since this particular inversion was performed using the discrepancy principle, the χ^2 misfit here is a diagnostic of successfully chosen regularization parameters, and here it is slightly larger than the total number of observed data (398) for the smallest value of damping.

to bottom, for the result shown in Figure 6a. The model covariance and correlation matrices show some significant correlation between certain parameters (for example, the first 10 parameters, which cover the south of the Southern Hemisphere, and parameters neighboring parameter number 30), and so they show a wide error distribution, also visible in Figure B2c. This correlation could be a consequence of poor data coverage in the Southern Hemisphere, while in the Northern Hemisphere it could be caused by many raypaths having the same direction. Since this particular inversion was performed using the L curve, χ^2 misfit in Figure B2d is just a measure of misfit rather than a diagnostic of successfully chosen regularization parameter like in the case of the discrepancy principle. For the discrepancy principle this value would have to be as close as possible to the total number of data used.

B2. Solution in Figure 6b

Using the data errors estimate from approach 1, we perform the inversion employing approach 2. The standard deviation of the t^* residuals was 0.38 for three repeats of the inversion using three damping parameters around the corner of the L curve, so it is the value we assumed for the noise of the data. Performing the inversion with that assumption and using the discrepancy principle to find the optimal damping parameter forces the algorithm to choose a very high damping parameter, resulting in a more heavily damped model. This is obvious as the majority of the parameters in that case takes on the value of the prior (not shown), and this is especially true for the parameters in the Southern Hemisphere. The confidence intervals, in that case, used to plot the uncertainty maps are relatively small, and consequently the lognormal distributions of the model parameters are narrow. While all of this is an expected behavior when the prior assumption dominates the inversion, the solution is overall too smooth which is not expected when using damping regularization. Increasing the value for the noise amplifies this issue resulting in an ever more damped solution. On the other hand, decreasing the noise value to 0.36 results in the solution shown in Figure 6b. This does, however, occur for minimum amount of damping (note the damping parameter and the corresponding χ^2

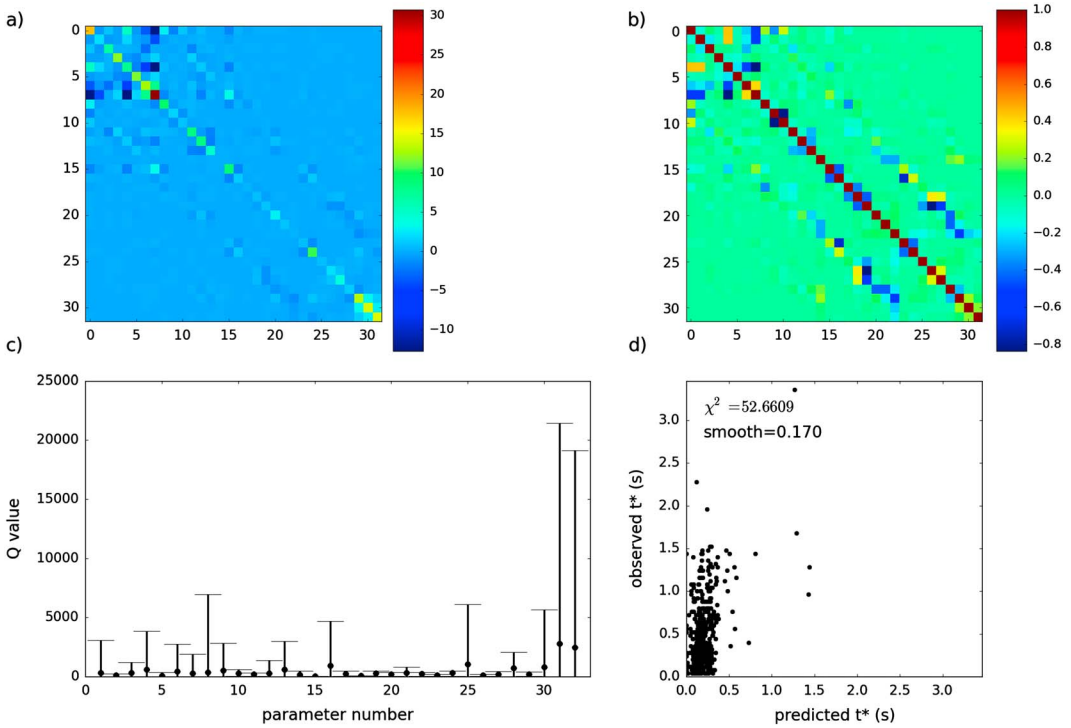

Figure B4. Inversion statistics corresponding to results from Figure 6c. (a) Model covariance matrix for parameters $\ln(Q_{p_i})$ shows high covariance between the 10–12 first parameters. All of these parameters are in the Southern Hemisphere where the ray coverage is poor. (b) Model correlation matrix computed directly from Figure B4a. It shows significant correlation between the first 10–12 parameters all located in the Southern Hemisphere but also for some of the parameters in the Northern Hemisphere. (c) The recovered Q_p model (black filled circles) and its 1σ confidence interval (error bars). (d) Observed data plotted as a function of predicted data. Also shown are the selected smoothing parameter of 0.17 and the χ^2 misfit between the observations and predictions. Since this particular inversion was performed using the L curve, χ^2 misfit here is just a measure of misfit rather than a diagnostic of successfully chosen regularization parameters like in the case of the discrepancy principle.

misfit in Figure B3d), suggesting that we cannot estimate data noise well in this case. The panels of Figure B3 show that in this case some of the parameters are estimated to be so large that it makes the confidence intervals hard to see. There is significant correlation between most of the parameters in the north and south, and this affects the inversion as a whole. We caution the reader that this solution shows a failed discrepancy principle approach.

The solution is nevertheless similar to the one shown in Figure 6a, so we take them as the optimal solutions for this problem and consider them to be the best possible solutions we can obtain with our data set.

Another reason to believe that these are indeed the best solutions obtained is the fact that we get similar optimal solutions for a significantly smaller noise estimate. For example, reducing the noise value to 0.1 did not change the overall optimal solution (not shown). It again was obtained with minimal amount of damping, and the χ^2 misfit was about 10 times larger than it should be. The only things that changed in that case are the estimated confidence intervals, which are all smaller. This makes sense, because in the Bayesian formulation smaller noise value means less noisy data, and consequently the predictions are in that sense better resolved, with smaller variance.

B3. Solution in Figure 6c

We computed the L curve again, using smoothing regularization (see Appendix A for differences between damping and smoothing) and chose a smoothing parameter from that curve. The L curve in this case looks similar to the one shown in Figure B1, and we chose our smoothing parameter α for this case to be 0.17. Using therefore approach 3 from Table 3, we obtain the solution shown in Figure 6c. The confidence intervals for one or two parameters are almost double the ones computed through damping (approach 1 and solution shown in Figure 6a). This is apparent through careful inspection of the covariance matrix and the confidence intervals of the optimal model shown in Figure B4. The patterns in the covariance and correlation matrices

Table 4. Seismic Networks Used in This Study and Their DOI Numbers[a]

Network Code	DOI/Operated by
AF	10.7914/SN/AF
AI	10.7914/SN/AI
AK	10.7914/SN/AK
AU	Geoscience Australia
BL	Universidade de Sao Paulo, USP
C	Universidad de Chile, Dept de Geofisica (DGF UChile Chile)
C1	Universidad de Chile, Dept de Geofisica (DGF UChile Chile)
CB	10.7914/SN/CB
CD	10.7914/SN/CD
CH	https://doi.org/10.12686/sed/networks/ch
CU	0.7914/SN/CU
CZ	10.7914/SN/CZ
DK	National Survey and Cadastre, Denmark
EI	10.7914/SN/EI
FR	https://doi.org/10.15778/RESIF.FR
G	10.18715/GEOSCOPE.G
GB	British Geological Survey, United Kingdom
GE	10.14470/TR560404
GR	Seismogisches Zentralobseratorium GRF, Germany
GT	10.7914/SN/GT
HL	10.7914/SN/HL
HT	10.7914/SN/HT
IC	10.7914/SN/IC
II	10.7914/SN/II
IU	10.7914/SN/IU
JP	JMA Japan Meteorological Agency
KN	Kyrgyz Institute of Seismology, IVTAN/KIS
KZ	10.7914/SN/KZ
MN	Istituto Nazionale di Geofisica e Vulcanologia (INGV), Italy
MS	Meteorological Service of Singapore
MY	Malaysian Meteorological Service
NL	ORFEUS (KNMI) Data Center, Royal Netherlands Meteorological Institute
OE	ZAMG - Central Institute for Meteorology and Geodynamics, Austria
PL	Polish Academy of Sciences (PAN) Polskiej Akademii Nauk
PM	Instituto Portugus do Mar e da Atmosfera, I.P. (IPMA), Portugal
PS	University of Tokyo, Earthquake Research Institute (Todai, ERI, Japan)
RO	10.7914/SN/RO
UK	University of Leicester (SEIS UK)
X4	10.7914/SN/X4_2016
XB	10.7914/SN/XB_1997
XB	10.7914/SN/XB_2000
XB	10.7914/SN/XB_2003
XB	10.7914/SN/XB_2005
XB	Woods Hole Oceanographic Institution (WHOI)
XB	10.7914/SN/XB_2009
XD	10.7914/SN/XD_1996
XD	10.7914/SN/XD_1999
XD	10.7914/SN/XD_2001

Table 4. (continued)

Network Code	DOI/Operated by
XD	IRIS/PASSCAL
XF	IRIS/PASSCAL
XG	IRIS/PASSCAL
XO	10.7914/SN/XO_1997
XO	10.7914/SN/XO_2003
XO	Stanford University
XO	Univeristy of Cambridge
XS	10.7914/SN/XS_2006
XS	Observatoire de Grenoble, Grenoble, France
YD	IRIS/PASSCAL
YG	University of Leeds (UK)
YI	IRIS/PASSCAL
YP	Rice University, United States
YT	Sismos a l'Ecole, Geosciences Azur, France
YW	University of Bristol (UK)
ZC	GEOFON Program (GFZ-Potsdam, Germany)
ZC	10.7914/SN/ZC_2006
ZC	10.7914/SN/ZC_2010
ZV	GEOFON Program (GFZ-Potsdam, Germany)
ZV	Woods Hole Oceanographic Institution (WHOI)
ZV	10.7914/SN/ZV_2007
ZV	10.7914/SN/ZV_2008

[a]Network operators are provided if DOI numbers are not.

are almost the same as those in Figure B2, and so are the majority of the values but for a few parameters. The lognormal probability distributions of each parameter are shown in Figure 8 and are also very similar to the ones shown in Figure 7.

Acknowledgments
The facilities of IRIS Data Services, and specifically the IRIS Data Management Center, were used for access to waveform and metadata required in this study. The IRIS DS is funded through the National Science Foundation and specifically the GEO Directorate through the Instrumentation and Facilities Program of the National Science Foundation under cooperative Agreement EAR-0004370. The authors would like to thank Brian L. N. Kennett, Phil Cummins, Ian Jackson, and two anonymous reviewers for discussions and their valuable comments. The list of seismic networks whose data we used in this study is given in Table 4. The final model and its uncertainties, shown in Figure 9, can be found in the supporting information.

References

Anderson, D. L., and R. S. Hart (1977), The *Q* of the Earth, *J. Geophys. Res.*, *83*(B12), 2156–2202.
Alboussière, T., R. Deguen, and M. Melzani (2010), Melting-induced stratification above the Earth's inner core due to convective translation, *Nature*, *466*, 744–747.
Aster, R., B. Borchers, and C. Thurber (2005), *Parameter Estimation and Inverse Problems, Int. Geophys. Ser.*, vol. 90, Elsevier, Amsterdam.
Attanayake, J., V. F. Cormier, and de Silva S. M. (2014), Uppermost inner core structure—New insights from body waveform inversion, *385*, 49–58, doi:10.1016/j.epsl.2013.10.025.
Aubert, J., H. Amit, G. Hulot, and P. Olson (2008), Thermochemical flows couple the Earth's inner core growth to mantle heterogeneity, *Nature*, *454*, 758–761.
Benavente, R. F. (2016), Rapid finite fault inversion for megathrust earthquakes, PhD thesis, Res. School of Earth Sci., College of Phys. and Math. Sci., The Australian Natl. Univ., Canberra, Australia.
Bhattacharyya, J., P. Shearer, and G. Masters (1993), Inner core attenuation from short-period PKP(Bc) versus PKP(Df) waveforms, *Geophys. J. Int.*, *114*, 1–11, doi:10.1111/j.1365-246x.1993.tb01461.x.
Cao, A., and B. Romanowicz (2004a), Constraints on density and shear velocity contrasts at the inner core boundary, *Geophys. J. Int.*, *157*, 1146–1151.
Cao, A., and B. Romanowicz (2004b), Hemispherical transition of seismic attenuation at the top of the Earth's inner core, *Earth Planet. Sci. Lett.*, *228*, 243–253, doi:10.1016/j.epsl.2004.09.032.
Carpenter, E. W. (1966), Absorption of elastic waves—An operator for a constant *Q* mechanism, *AWRE Rep. No. 0-43/66*, H. M. Stationary Off., London.
Chevrot, S. (2002), Optimal waveform and delay time analysis by simulated annealing, *Geophys. J. Int*, *151*, 164–171.
Cormier, V. F. (1981), Short period PKP and the anelastic mechanism of the inner core, *Phys. Earth Planet. Inter.*, *24*, 291–301.
Creager, K. C. (1999), Large-scale variations in inner core anisotropy, *J. Geophys. Res.*, *104*, 23127–23139.
Deguen, R., T. Alboussière, and P. Cardin (2013), Thermal convection in Earth's inner core with phase change at its boundary, *Geophys. J. Int.*, *194*(3), 1310–1334, doi:10.1093/gji/ggt202.
Doornbos, D. J. (1974), The anelasticity of the inner core, *Geophys. J. Int.*, *38*, 397–415.
Doornbos, D. J. (1983), Observable effects of the seismic absorption band in the Earth, *Geophys. J. Int.*, *75*, 693–711.
Futterman, W. I. (1962), Dispersive body waves, *J. Geophys. Res.*, *67*, 5279–5291.

Garcia, R., S. Chevrot, and M. Weber (2004), Nonlinear waveform and delay time analysis of triplicated core phases, *J. Geophys. Res.*, *109*, B01306, doi:10.1029/2003JB002429.
Garcia, R., L. Shardong, and S. Chevrot (2013), A nonlinear method to estimate source parameters, amplitude, and travel times of teleseismic body waves, *Bull. Seismol. Soc. Am.*, *103*, 268–282.
Gomi, H., and K. Hirose (2015), Electrical resistivity and thermal conductivity of hcp Fe-Ni alloys under high pressure: Implications for thermal convection in the Earth's core, *Phys. Earth Planet. Inter.*, *247*, 2–10.
Gubbins, D., B. Sreenivasan, J. Mound, and S. Rost (2011), Melting of the Earth's inner core, *Nature*, *473*, 361–364.
Hansen, P. C. (1992), Analysis of discrete ill-posed problems by means of the L-curve, *SIAM Rev.*, *34*, 561–580.
Iritani, R., N. Takeuchi, and H. Kawakatsu (2010), Seismic attenuation structure of the top half of the inner core beneath the northeastern Pacific, *Geophys. Res. Lett.*, *37*, L19303, doi:10.1029/2010GL044053.
Iritani, R., N. Takeuchi, and H. Kawakatsu (2014a), Intricate heterogeneous structures of the top 300 km of the Earth's inner core inferred from global array data: I. Regional 1D attenuation and velocity profiles, *Phys. Earth Planet. Inter.*, *230*, 15–27, doi:10.1016/j.pepi.2014.02.002.
Iritani, R., N. Takeuchi, and H. Kawakatsu (2014b), Intricate heterogeneous structures of the top 300 km of the Earth's inner core inferred from global array data: II. Frequency dependence of inner core attenuation and its implication, *Earth Planet. Sci. Lett.*, *405*, 231–243, doi:10.1016/j.epsl.2014.08.038.
Irving, J. C. E., and A. Deuss (2011), Hemispherical structure in inner core velocity anisotropy, *J. Geophys. Res.*, *116*, B04307, doi:10.1029/2010JB007942.
Kennett, B., E. Engdahl, and R. Buland (1995), Constraints on seismic velocities in the Earth from traveltimes, *Geophys. J. Int.*, *122*, 108–124.
Li, X., and V. F. Cormier (2002), Frequency-dependent seismic attenuation in the inner core, 1. A viscoelastic interpretation, *J. Geophys. Res.*, *107*(B12), 2361, doi:10.1029/2002JB001795.
Monnereau, M., M. Calvet, L. Margerin, and A. Souriau (2010), Lopsided growth of Earth's inner core, *Science*, *328*, 1014–1017.
Niazi, M., and L. R. Johnson (1992), Q in the inner core, *Phys. Earth Planet. Inter.*, *74*, 55–62.
Niu, F., and L. Wen (2001), Hemispherical variations in seismic velocity at the top of the Earth's inner core, *Nature*, *410*, 1081–1084.
Pozzo, M., C. Davies, D. Gubbins, and D. Alfè (2014), Thermal and electrical conductivity of solid iron and iron-silicon mixtures at Earth's core conditions, *Earth Planet. Sci. Lett.*, *393*, 159–164.
Shearer, P., and G. Masters (1990), The density and shear velocity contrast at the inner core boundary, *Geophys. J. Int.*, *102*, 491–498.
Singh, S. C., M. A. J. Taylor, and J. P. Montagner (2002), On the presence of liquid in Earth's inner core, *Science*, *287*, 2471–2474.
Sivia, D. S., and J. Skilling (2006), *Data Analysis: A Bayesian Tutorial*, Oxford Univ. Press, New York.
Souriau, A., and B. Romanowicz (1996), Anisotropy in the inner core: Relation between P-velocity and attenuation, *Phys. Earth Planet. Inter.*, *101*, 33–47.
Souriau, A., and P. Roudil (1995), Attenuation in the uppermost inner core from broad-band GEOSCOPE PKP data, *Geophys. J. Int.*, *123*, 572–587.
Tanaka, S. (2012), Depth extent of hemispherical inner core from PKP(DF) and PKP(Cdiff) for equatorial paths, *Phys. Earth Planet. Inter.*, *210–211*, 50–62, doi:10.1016/j.pepi.2012.08.001.
Tanaka, S., and H. Hamaguchi (1997), Degree one heterogeneity and hemispherical variation of anisotropy in the inner core from PKP(BC)-PKP(DF) times, *J. Geophys. Res.*, *102*, 2925–2938, doi:10.1029/96JB03187.
Tkalčić, H. (2015), Complex inner core of the Earth: The last frontier of global seismology, *Rev. Geophys.*, *53*, 59–94, doi:10.1002/2014RG000469.
Wen, L., and F. Niu (2002), Seismic velocity and attenuation structures in the top of the Earth's inner core, *J. Geophys. Res.*, *107*(B11), 2273, doi:10.1029/2001JB000170.
Yu, W., and L. Wen (2006), Seismic velocity and attenuation structures in the top 400 km of the Earth's inner core along equatorial paths, *J. Geophys. Res.*, *111*, B07308, doi:10.1029/2005JB003995.